



# A crystal plasticity FE model for deformation with twin nucleation in magnesium alloys

Jiahao Cheng, Somnath Ghosh\*

Departments of Civil and Mechanical Engineering, Johns Hopkins University, United States

## ARTICLE INFO

### Article history:

Received 2 July 2014

Received in final revised form 27 September 2014

Available online 22 October 2014

### Keywords:

A. Dislocations

A. Twinning

B. Crystal plasticity

B. Polycrystalline material

C. Finite elements

## ABSTRACT

Magnesium alloys exhibit complex deformation related mechanical behavior, viz. plastic anisotropy, tension–compression asymmetry and premature failure. Their origins are in the underlying heterogeneous deformation due to dislocation slip and micro-twin formation on different crystallographic systems. Reliable prediction of mechanical response and failure is predicated upon the ability of computational models of polycrystalline microstructures to accurately simulate such deformational heterogeneity and localization. In this paper a physically-motivated non-local crystal plasticity finite element (CPFE) model is developed for dislocation-mediated heterogeneous deformation of single and polycrystalline Mg alloys leading to micro-twin nucleation. The CPFE model uses image-based virtual polycrystalline microstructures for its simulations and is able to effectively represent stress and deformation patterns in the intra- and inter-granular regions. A micro-twin nucleation criteria is proposed from energy-partitioning following the dislocation dissociation process. The CPFE simulations of polycrystalline microstructures show satisfactory agreement with experimental observations. CPFEM studies on large grain aggregates using this criteria, reveal the critical role of crystallographic orientation and grain boundaries on micro-twin formation.

© 2014 Elsevier Ltd. All rights reserved.

## 1. Introduction

The quest for low density, high strength and durable materials in high performance automotive and aerospace applications has resulted in magnesium alloys as candidate materials with high potential (Bettles and Gibson, 2005; Kainer, 2003). The density of magnesium is about 23% that of steel and 66% that of aluminum, while its weight for equivalent bending stiffness is 62% less than steel and 23% less than aluminum. Being among the lightest of structural metals with high stiffness and strength at a range of temperatures, these alloys can offer considerably increased component strength to weight ratio. These desirable properties can have the ultimate consequences of significant savings in energy consumption and reduction in CO<sub>2</sub> emissions. An important consideration in the processing and high performance industrial applications of Mg alloys is their deformation behavior and failure characteristics at a range of strain rates and temperatures. Of particular interest is their ductility properties, e.g. their behavior in forming processes like extrusion or rolling, or under impact loads as in crashworthiness tests. Understanding the physics of the plastic deformation and failure of magnesium alloys is therefore essential for tailoring their ductility, especially at room temperatures.

\* Corresponding author at: 3400 N. Charles St., Baltimore, MD 21218, United States. Tel.: +1 410 516 7833; fax: +1 410 516 7473.  
E-mail address: [sghosh20@jhu.edu](mailto:sghosh20@jhu.edu) (S. Ghosh).

A complicating phenomenon of magnesium and its alloys (e.g., AZ31) is their deformation induced anomalous mechanical behavior (Kaiser et al., 2003; Bohlen et al., 2007; Barnett, 2007a,b; Brown et al., 2007; Ma et al., 2011; Kadiri et al., 2013). These materials possess low-symmetry hexagonal closed packed (*hcp*) crystallographic structure, an attribute that leads to pronounced anisotropy in mechanical properties, e.g. tension–compression asymmetry of the yield strength. Low symmetry results in a variety of slip systems for the *hcp* crystalline lattice, shown in Fig. 1. At low temperatures, the critical resolved shear stress (CRSS) is much lower for basal slip  $(0001) \langle 11\bar{2}0 \rangle$ , than it is for prismatic  $\{10\bar{1}0\} \langle 11\bar{2}0 \rangle$  or pyramidal  $\{11\bar{2}2\} \langle 11\bar{2}3 \rangle$  slip systems. Only the basal  $\langle a \rangle$  slip can occur under low applied stresses. Any deformation involving changes in the  $\langle c \rangle$  direction ensues a competition between the high CRSS  $\langle c+a \rangle$  slip systems and the less understood micro-twin mechanisms (Duygulu and Agnew, 2005). The myriad of interactions among slip and twin systems lead to complex plastic behavior, involving plastic anisotropy, tension–compression asymmetry and premature failure. Local stress and dislocation concentrations at locations of microstructural heterogeneities in polycrystalline aggregates close to grain boundaries with strong texture and grain size distribution are responsible for this behavior. It is important to develop physics-based models of deformation and micro-twinning in Mg alloys with the goal of understanding the effect of microstructure on failure.

Major computational approaches have been developed for continuum-scale simulation of polycrystal aggregates of Mg alloys. The elasto-visco-plastic self-consistent or EVPSC method started in (Hutchinson, 1976), evolved in (Molinari et al., 1987) and was further developed in (Lebensohn and Tome, 1993, 1994) to account for large anisotropic viscoplastic deformation. Features like dislocation slip inside a twin band, detwinning, effect of solid solution and dislocation transmutation caused twin hardening have been included for *hcp* crystals in recent developments (Proust et al., 2009; Wang et al., 2012; Raeisinia and Agnew, 2010; Kadiri and Oppedal, 2010; Oppedal et al., 2012). In the EVPSC scheme, each grain is treated as an ellipsoidal inclusion embedded in a homogeneous medium representing the averaged behavior of all other grains, while preserving equilibrium and compatibility. It is an efficient method for modeling the behavior and texture evolution of large grain aggregates. Grains however are not in direct interaction with their neighbors, and the effect of grain boundary, grain shape and stress heterogeneity inside each grain are not explicitly represented. Crystal plasticity finite element models or CPFEM have been implemented to model deformation in Mg alloys in (Staroselsky and Anand, 2003; Graff et al., 2007; Izadbakhsh et al., 2011, 2012; Zhang and Joshi, 2012; Abdolvand and Daymond, 2013). A non-local constitutive model has been developed by (Ma et al., 2006) for CPFEM with the emphasis on accumulation of geometrically necessary dislocations (GNDs).

Modeling deformation twinning is a key to effective failure prediction for Mg alloys. The formation of micro-twins is facilitated by the low number of easy slip systems in *hcp* metals. However, a number of important fundamental questions remain, e.g. how does a micro-twin nucleate, how the twin boundary migrate or when does a grain saturate with accommodating twins. The formation of micro-twins by the nucleation and glide of twinning dislocations are not on close packing planes as discussed in (Serra et al., 1991). The glide of twin dislocations not only provides shear deformation but also requires a collaborative shuffling of atoms over more than one crystallographic plane (Hirth and Lothe, 1982). This non-planar atomic shuffling, together with twin shear, reorients the initial crystallographic lattice in a mirror-symmetry and thickens the twin. Two types of twin nucleation theories, referred to as homogeneous and heterogeneous theories, have been proposed for *hcp* metals. The homogeneous theory (Koehler et al., 1954) assumes nucleation from a perfect crystal lattice, while the heterogeneous theory (Mendelson, 1970; Capolungo and Beyerlein, 2008; Beyerlein and Tome, 2010; Ghazisaeidi and Curtin, 2013) considers the effect of existing defects and microstructure on twinning. The homogeneous models require very high stress levels, close to material's theoretical strength, which can only happen in extreme loading conditions. The heterogeneous models are more suited for micro-twinning under lower-strain rate and quasi-static loading conditions. Beyerlein and Tome (2010) considered the twin nucleation from defects at low angle grain boundaries.

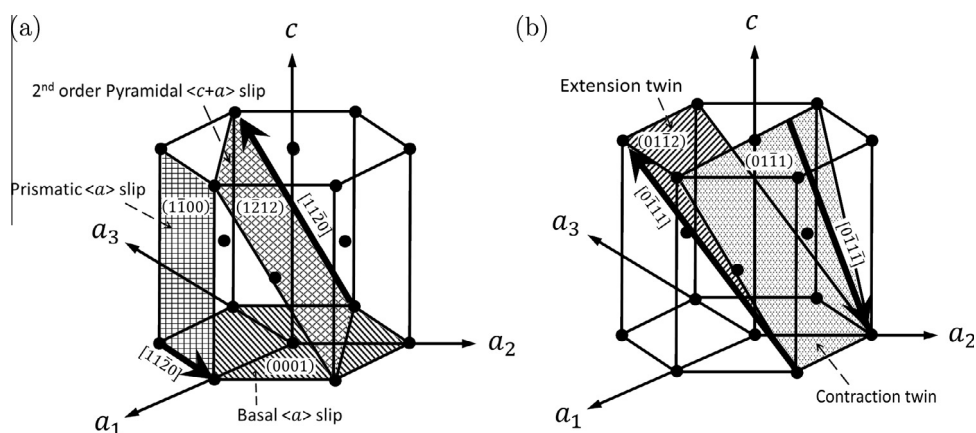


Fig. 1. Schematic showing: (a) active slip systems and (b) twin systems in *hcp* magnesium alloys.

Thompson and Millard (1952) introduced a “pole mechanism”, which considers the coplanar dissociation of  $\langle c \rangle$  lattice dislocations as a source of twinning. This was extended in (Mendelson, 1970) using linear elasticity theory to incorporate the dissociation of a  $\langle a \rangle$ ,  $\langle c \rangle$  or  $\langle c + a \rangle$  dislocation into one or more glissile twinning dislocation loops and a sessile stair-rod dislocation, lying between the slip plane of the original dislocation and twin planes. In (Capolungo and Beyerlein, 2008) it has been shown that it is not possible to form a stable twin unless it is at the head of a dislocation pileup. Studies on the dissociation of  $\langle c \rangle$  and  $\langle c + a \rangle$  type dislocation into  $n$  layer  $\{10\bar{1}2\}$  twins in (Ghazisaeidi and Curtin, 2013) have found them to be feasible mechanisms for nucleation of  $\{10\bar{1}2\}$  tension twins.

The present paper develops a CPFEM model for dislocation-mediated heterogeneous deformation of single and polycrystalline Mg alloy microstructures that leads to micro-twin nucleation. The non-local model implemented in this work captures local stress concentrations near soft-hard grain boundaries due to accumulation of geometrically necessary dislocations. In Section 2 a crystal plasticity constitutive model is developed for dislocation glide and accumulation that is numerically implemented in a CPFEM framework. Section 3 discusses the method of calibrating model parameters using genetic algorithms from experimental data on single crystal pure Mg. The CPFEM model is validated for real microstructures of polycrystalline Mg alloy AZ31 in Section 4. Section 5 is devoted to the development of a micro-twin nucleation in polycrystalline microstructures and detailed study on the effect of microstructure on twin nucleation. The paper summarizes the developments in Section 6.

## 2. Crystal plasticity constitutive model of slip-mediated deformation

Mg alloys, e.g. the wrought alloy AZ31, possess low-symmetry hexagonal closed packed (*hcp*) crystallographic structure, consisting of 5 different families of slip systems, namely the basal  $\langle a \rangle$ , prismatic  $\langle a \rangle$ , pyramidal  $\langle a \rangle$ , first order pyramidal  $\langle c + a \rangle$  and second order pyramidal  $\langle c + a \rangle$  with a total of 30 slip systems. Pronounced differences are generally found in the critical resolved shear stresses and strain-hardening rates in the different slip systems, causing strong anisotropy in mechanical properties such as tension–compression asymmetry of the yield strength. Experimental observations for Mg alloys e.g. in (Kelley and Hosford, 1968) have indicated that only 12 slip systems are generally active, while others like the first-order pyramidal slip system tend to dissociate and are rarely active in dislocation glide (Li and Ma, 2009). Consequently for efficiency, the present model considers 3 basal slip modes  $(0001)\langle 11\bar{2}0 \rangle$ , 3 prismatic slip modes  $\{10\bar{1}0\}\langle 11\bar{2}0 \rangle$  and 6 second order pyramidal  $\langle c + a \rangle$  slip modes  $\{11\bar{2}2\}\langle 11\bar{2}3 \rangle$  in 12 slip systems (Graff et al., 2007; Ma et al., 2012). A schematic of the slip and twin systems in the *hcp* magnesium alloys is shown in Fig. 1. The crystal plasticity constitutive model is adapted from the size and time dependent, finite strain models that have been developed for Ti alloys in (Hasiija et al., 2003; Deka et al., 2006; Venkataramani et al., 2007, 2008; Anahid et al., 2011; Ghosh and Chakraborty, 2013). Expressions for the slip system deformation resistance evolution and back-stress evolution in the phenomenological power-law model are enhanced by more physics-based thermally activated obstacle to slip and athermal obstacles, which correspond to the cutting and passing stress barriers respectively (Keshavarz and Ghosh, 2013). The crystal plasticity model accounts for microstructural features such as hardening due to statistically stored dislocation and geometrically necessary dislocation densities. Furthermore, the modeling of deformation twinning in polycrystalline microstructures is incorporated in Section 5.

### 2.1. Crystal plasticity constitutive relations

Following conventional developments of crystal plasticity theory in (Peirce et al., 1983, 1982), the total deformation gradient is assumed to admit a multiplicative decomposition as:

$$\mathbf{F} = \mathbf{F}^e \mathbf{F}^p, \quad \det(\mathbf{F}^e) > 0 \quad (1)$$

where  $\mathbf{F}$  is the deformation gradient tensor,  $\mathbf{F}^e$  is its elastic component that describes stretching and rotation of the crystal lattice, and  $\mathbf{F}^p$  is its incompressible plastic component, i.e.  $\det(\mathbf{F}^p) = 1$ . The decomposition admits an anholonomic unstressed intermediate configuration  $B_i$  associated with the population and motion of crystal defects, for which  $\mathbf{F}^e$  is associated with the driving stress that brings  $B_i$  to the current configuration  $B_c$ . The stress–strain constitutive equation in the reference configuration is written in terms of the second Piola–Kirchhoff stress tensor  $\mathbf{S}$  and its work-conjugate Lagrange–Green strain tensor  $\mathbf{E}^e$  as:

$$\mathbf{S} = \mathbf{C} : \mathbf{E}^e \quad \text{where} \quad \mathbf{E}^e = \frac{1}{2}(\mathbf{F}^{eT} \mathbf{F}^e - \mathbf{I}) \quad (2)$$

where  $\mathbf{C}$  is a fourth order anisotropic elasticity tensor. Plastic deformation of magnesium alloys at moderate strain-rates is predominantly caused by dislocation glide on selected slip systems and micro-twin evolution. The flow rule, governing evolution of plastic deformation due to dislocations, is expressed in terms of the plastic velocity gradient  $\mathbf{L}^p$  as:

$$\mathbf{L}^p = \dot{\mathbf{F}}^p \mathbf{F}^{p-1} = \sum_{\alpha}^{nslip} \dot{\gamma}^{\alpha} \mathbf{s}_0^{\alpha} \quad (3)$$

where  $\dot{\gamma}^{\alpha}$  is the slip rate on the  $\alpha$  slip system and  $nslip$  is the total number of active slip systems. The Schmid tensor associated with  $\alpha$ -th slip system  $\mathbf{s}_0^{\alpha}$  is expressed in terms of the slip direction  $\mathbf{m}_0^{\alpha}$  and slip plane normal  $\mathbf{n}_0^{\alpha}$  in the unrotated

reference configuration  $B_i$  as  $\mathbf{s}_0^\alpha = \mathbf{m}_0^\alpha \otimes \mathbf{n}_0^\alpha$ . Combining the models in (Anahid et al., 2011; Ghosh and Chakraborty, 2013; Keshavarz and Ghosh, 2013) the plastic slip rate  $\dot{\gamma}^\alpha$  on the  $\alpha$ -th slip system has a power law dependence on the resolved shear stress  $\tau^\alpha$  from the far-field stress, and the slip system deformation resistances overcoming the local thermal and athermal barriers. This can be expressed as:

$$\dot{\gamma}^\alpha = \dot{\gamma}_0^\alpha \left| \frac{\tau^\alpha - s_a^\alpha}{s_*^\alpha} \right|^{\frac{1}{m}} \text{sign}(\tau^\alpha - s_a^\alpha) \quad (4)$$

Here, the temperature-dependent critical shear resistance  $s^\alpha$  is assumed to be comprised of a thermally activated obstacle to slip  $s_*^\alpha$  and a part due to the athermal obstacles  $s_a^\alpha$ . The athermal resistance arises from the long-range internal stress field between parallel dislocation lines or from grain boundaries, while the thermal shear resistance is due to local obstacles caused by particles, dislocation jogs or forest dislocations.  $s_a^\alpha$  and  $s_*^\alpha$  correspond to the passing and cutting stress barriers respectively, with the driving force for dislocation motion on the slip system being the difference between the resolved shear stress and athermal shear resistance. The term  $\tau^\alpha - s_a^\alpha$  is the local effective driving force applied on a dislocation line. The resolved shear stress on a slip system  $\tau^\alpha$  is derived as:

$$\tau^\alpha = (\mathbf{F}^{\alpha T} \mathbf{F}^\alpha \mathbf{S}) : (\mathbf{s}_0^\alpha) \quad (5)$$

The exponent  $m$  corresponds to the strain-rate sensitivity,  $\dot{\gamma}_0^\alpha$  is the reference slip rate for  $\alpha$  system.

The power law model of Eq. (4) is consistent with the activation energy based model (Kock et al., 1975) of the form:

$$\dot{\gamma}^\alpha = \dot{\gamma}_0^\alpha \exp \left\{ -\frac{1}{k_B T} \Delta F_* \left[ 1 - \left( \frac{|\tau^\alpha - s_a^\alpha|}{s_*^\alpha} \right)^p \right]^q \right\} \text{sign}(\tau^\alpha - s_a^\alpha) \quad (6)$$

where parameters  $p$  and  $q$  correspond to the shape of local obstacles and  $\Delta F_*$  is the thermal activation energy. For cuboidal shapes of local obstacles,  $p = q = 1$ . Moreover, for moderate rates of plastic deformation regime the factor  $\frac{|\tau^\alpha - s_a^\alpha|}{s_*^\alpha}$  is of the order  $\mathcal{O}(1)$ , for which the exponential term  $\exp \left( \frac{|\tau^\alpha - s_a^\alpha|}{s_*^\alpha} - 1 \right)$  can be expanded in a series while retaining only the linear term  $\frac{|\tau^\alpha - s_a^\alpha|}{s_*^\alpha}$ . Correspondingly, the exponent in Eq. (4) may be equated as  $\frac{1}{m} = \frac{\Delta F_*}{k_B T}$ , which for magnesium and its alloys has a value typically larger than 30 (Kim et al., 2000). In the present work, an isothermal assumption is made, for which the value of the power-law exponent  $\frac{1}{m}$  is constant.

### 2.1.1. Evolution of slip system resistance

The evolution of shear resistance on individual slip systems is governed by two types of dislocations, viz. statistical stored dislocations (SSDs) and geometrically necessary dislocations (GNDs) (Ashby, 1970; Ma et al., 2006; Ghosh and Chakraborty, 2013). The accommodation of SSDs, which correspond to homogeneous plastic deformation that is characterized by vanishing net Burgers vector, is the result of random trapping and multiplication process in chance encounters. The existence of GNDs corresponds to the storage of polarized dislocation densities, necessary to accommodate the crystal lattice curvature such as in single crystal bending or near polycrystalline grain boundaries. Phenomenological hardening laws, proposed in (Keshavarz and Ghosh, 2013), are assumed for the evolution of thermal and athermal shear resistances contributing to the overall shear resistance. The thermal shear resistance  $s_a^\alpha$  accounts for the effect of forest dislocations normal to  $\alpha$  slip plane, while the athermal shear resistance  $s_*^\alpha$  reflects the effect of parallel dislocations in the slip direction  $\mathbf{m}^\alpha$ . They are constituted of three components, viz. the initial shear resistance and contributions due to the evolution of the SSDs and GNDs respectively, i.e.  $s_{a/*}^\alpha = s_{a/*,0}^\alpha + s_{a/*,SSD}^\alpha + s_{a/*,GND}^\alpha$ . For SSDs, the rate of evolution of these resistances are expressed as:

$$\dot{s}_{a,SSD}^\alpha = \sum_{\beta=1}^N h_a^{\alpha\beta} |\dot{\gamma}^\beta \sin(\mathbf{n}^\alpha, \mathbf{t}^\beta)| \quad (7a)$$

$$\dot{s}_{*,SSD}^\alpha = \sum_{\beta=1}^N h_*^{\alpha\beta} |\dot{\gamma}^\beta \cos(\mathbf{n}^\alpha, \mathbf{t}^\beta)| \quad (7b)$$

where  $\mathbf{n}^\alpha$  is the normal to the slip system plane  $\alpha$  and  $\mathbf{t}^\beta$  is the dislocation line tangent vector for edge dislocation on the slip plane  $\beta$ . It is derived as the cross product of the slip direction and slip plane normal, i.e.  $\mathbf{t}^\beta = \mathbf{m}^\beta \times \mathbf{n}^\beta$ . Eq. (7a) corresponds to the projection of  $\beta$  slip system dislocations parallel to the  $\alpha$  slip plane, while Eq. (7b) projects them on a plane normal to  $\alpha$  slip plane. In this work, SSDs due to edge dislocations are considered only (Ma et al., 2006; Keshavarz and Ghosh, 2013). To incorporate the contribution of screw dislocations in SSDs e.g. in (Castany et al., 2008) for Ti6Al4V alloys, the direction of the dislocation line tangent vector should be  $\mathbf{m}^\beta$ , and the projection relations in Eqs. (7) should additionally incorporate the projection angle corresponding to  $(\mathbf{n}^\alpha, \mathbf{m}^\beta)$ . Moduli  $h_a^{\alpha\beta}$  and  $h_*^{\alpha\beta}$  describe strain hardening rate due to both self and latent hardening on the slip system  $\alpha$  due to slip on the slip system  $\beta$ . The hardening moduli for athermal and thermal shear resistances are assumed to be identical in this work, i.e.

$$h_a^{\alpha\beta} = h_*^{\alpha\beta} = q^{\alpha\beta} h^\beta, \quad (\text{no sum on } \beta) \quad (8)$$

Here  $h^\beta$  is the self-hardening coefficient on the slip system  $\beta$  and  $q^{2\beta}$  is a matrix describing latent hardening. The evolution of self hardening rate is expressed as:

$$h^\beta = h_{ref}^\beta \left| 1 - \frac{s^\beta}{s_{sat}^\beta} \right|^r \text{sign} \left( 1 - \frac{s^\beta}{s_{sat}^\beta} \right) \quad (9)$$

where the exponent  $r$  is a material constant and  $s_{sat}^\beta$  is the reference value of saturation stress on  $\beta$  slip system. The magnitude of the total shear resistance is given as  $s^\beta = \sqrt{(s_a^\beta)^2 + (s_s^\beta)^2}$ .

The consideration of hardening due to geometrically necessary dislocations or GNDs is important for *hcp* crystals that exhibit anisotropy due to a high degree of heterogeneity between different slip systems. Grains with different orientations have significant differences in response under loading that result in lattice curvatures and accumulation of GNDs at grain boundaries. They are necessary for providing additional stresses to maintain compatibility at grain boundaries. The components of GNDs may be derived from the Nye's dislocation density tensor  $\Lambda$ , which measures the incompatibility in the intermediate configuration and is expressed as (Arsenlis, 2001):

$$\Lambda = -(\nabla_X \times \mathbf{F}^{\beta T})^T \quad (10)$$

where  $\nabla_X$  is the gradient operator with respect to the reference coordinates. Both edge and screw components of GNDs contribute to  $\Lambda$  in the incompatible intermediate configuration (Ma et al., 2006). Thus the GNDs on each slip system are decomposed into three groups, viz. one group of screw components  $\rho_{GND,s}^\alpha$  with their line tangent vector parallel to the slip direction  $\mathbf{m}^\alpha$ , and two groups of edge components  $\rho_{GND,en}^\alpha$  and  $\rho_{GND,et}^\alpha$  with their respective line tangent vectors parallel to slip plane normal  $\mathbf{n}^\alpha$  and  $\mathbf{t}^\alpha = \mathbf{m}^\alpha \times \mathbf{n}^\alpha$ . This may be written as:

$$\Lambda = \sum_{\alpha=1}^{nslip} \rho_{GND,s}^\alpha \mathbf{b}^\alpha \otimes \mathbf{m}^\alpha + \rho_{GND,et}^\alpha \mathbf{b}^\alpha \otimes \mathbf{t}^\alpha + \rho_{GND,en}^\alpha \mathbf{b}^\alpha \otimes \mathbf{n}^\alpha \quad (11)$$

where  $nslip = 12$ , and  $\mathbf{b}^\alpha$  is the Burgers vector on the slip system  $\alpha$ . Eqs. (10) and (11) constitute an under-constrained problem, in which 36 independent components of  $\rho_{GND}^\alpha$ , viz. 12  $\rho_{GND,s}^\alpha$ , 12  $\rho_{GND,et}^\alpha$  and 12  $\rho_{GND,en}^\alpha$  need to be solved from 9 equations. Eq. (11) may be written in a matrix form as:

$$\{\widehat{\Lambda}\} = [\mathbf{A}]\{\rho_{GND}\} \quad (12)$$

where  $\{\widehat{\Lambda}\}$  is  $9 \times 1$  vector form of the Nye's dislocation density tensor  $\Lambda$ ,  $[\mathbf{A}]$  is a  $9 \times 36$  linear operator matrix containing the basis tensors  $\mathbf{b}^\alpha \otimes \mathbf{m}^\alpha$ ,  $\mathbf{b}^\alpha \otimes \mathbf{t}^\alpha$  and  $\mathbf{b}^\alpha \otimes \mathbf{n}^\alpha$ , and  $\{\rho_{GND}\}$  is the  $36 \times 1$  vector column of GND components. Eq. (12) yields an under-determined system of linear equations that has an infinite solutions, if any. Consequently, following discussions in (Arsenlis and Parks, 1998), a minimization problem is solved for the  $L_2$  norm of the GND density (see below) subject to the constraints of Eq. (12). The  $L_2$  norm is expressed as the sum of the squares of GND densities on each slip system as:

$$\{\rho_{GND}\}^T \{\rho_{GND}\} = \sum_{\alpha} (\rho_{GND,s}^\alpha)^2 + (\rho_{GND,et}^\alpha)^2 + (\rho_{GND,en}^\alpha)^2 = \sum_{\alpha} (\rho_{GND}^\alpha)^2 \quad (13)$$

Geometric constraints posed in Eq. (12) allows only certain dislocations to exist on the slip planes, which is taken into account by minimizing the functional of the form:

$$\mathcal{F}(\{\rho_{GND}\}, \{\lambda\}) = \left\{ \{\rho_{GND}\}^T \{\rho_{GND}\} + \{\lambda\}^T ([\mathbf{A}]\{\rho_{GND}\} - \{\widehat{\Lambda}\}) \right\} \quad (14)$$

Here  $\{\lambda\}$  is a  $9 \times 1$  column vector containing components of the Lagrange multipliers. The stationarity conditions  $\frac{\partial \mathcal{F}}{\partial (\rho_{GND})} = 0$  and  $\frac{\partial \mathcal{F}}{\partial (\lambda)} = 0$  yield the equation to be solved:

$$\{\rho_{GND}\} = [\mathbf{A}]^T ([\mathbf{A}][\mathbf{A}]^T)^{-1} \{\widehat{\Lambda}\} \quad (15)$$

The GNDs contribute to slip system resistance through increase in the long-range passing stress due to the interaction of mobile dislocations with parallel dislocations, as well as increase in cutting stress due to mobile dislocations cutting the forest dislocations perpendicular to the slip plane. Parallel and forest dislocation densities due to the GNDs may be expressed in terms of the components as (Ma et al., 2006):

$$\rho_{GND,P}^\alpha = \sum_{\beta=1}^{nslip} \chi^{\alpha\beta} \left[ \rho_{GND,s}^\beta |\sin(\mathbf{n}^\alpha, \mathbf{m}^\beta)| + \rho_{GND,et}^\beta |\sin(\mathbf{n}^\alpha, \mathbf{t}^\beta)| + \rho_{GND,en}^\beta |\sin(\mathbf{n}^\alpha, \mathbf{n}^\beta)| \right] \quad (16a)$$

$$\rho_{GND,F}^\alpha = \sum_{\beta=1}^{nslip} \chi^{\alpha\beta} \left[ \rho_{GND,s}^\beta |\cos(\mathbf{n}^\alpha, \mathbf{m}^\beta)| + \rho_{GND,et}^\beta |\cos(\mathbf{n}^\alpha, \mathbf{t}^\beta)| + \rho_{GND,en}^\beta |\cos(\mathbf{n}^\alpha, \mathbf{n}^\beta)| \right] \quad (16b)$$

The coefficient  $\chi^{\alpha\beta}$  describes the strengthening effect due to the interaction between  $\alpha$  slip system and  $\beta$  slip system, e.g. in the formation of dislocation locks. For *hcp* crystals  $\chi^{\alpha\beta}$  is taken as 1 in this work. As noted in (Ma et al., 2006), Eq. (16) uses the

absolute value of GND density without accounting for the sign of Burgers vector, which may result in a loss of the kinematic hardening due to GNDs. The athermal and thermal shear resistances from GND hardening at time  $t$  are expressed as:

$$s_{a,GND}^{\alpha} = c_1 G b^{\alpha} \sqrt{\rho_{GND,P}^{\alpha}} \quad \text{and} \quad s_{*,GND}^{\alpha} = \frac{Q_{slip}^{\alpha}}{c_2 c_3 b^{\alpha 2}} \sqrt{\rho_{GND,F}^{\alpha}} \quad (17)$$

where the athermal shear resistance is from the long-range internal stress field between mobile dislocation lines on  $\alpha$  slip system and parallel GNDs and the thermal shear resistance arises from mobile dislocation cutting forest GNDs. Here  $G$  is the shear modulus,  $c_1$  is a constant for passing stress,  $c_2$  is a constant for jump width,  $c_3$  is a constant for obstacle width,  $b^{\alpha}$  is the magnitude of Burgers vector for  $\alpha$  slip system and  $Q_{slip}^{\alpha}$  is the effective activation energy for dislocation slip. In this work, an approximation that  $Q_{slip}^{\alpha} = 10 G b^{\alpha 2}$  is made for *hcp* crystals. Adding all contributions, the thermal and athermal shear resistance with both SSD and GND hardening at time  $t$  are expressed as:

$$s_a^{\alpha} = s_{a,0}^{\alpha} + \int_{t'=0}^{t'=t} \sum_{\beta=1}^{nslip} h^{\alpha\beta} |\dot{\gamma}^{\beta}| \sin(\mathbf{n}^{\alpha}, \mathbf{t}^{\beta}) dt' + c_1 G b^{\alpha} \sqrt{\rho_{GND,P}^{\alpha}} \quad (18a)$$

$$s_*^{\alpha} = s_{*,0}^{\alpha} + \int_{t'=0}^{t'=t} \sum_{\beta=1}^{nslip} h^{\alpha\beta} |\dot{\gamma}^{\beta}| \cos(\mathbf{n}^{\alpha}, \mathbf{t}^{\beta}) dt' + \frac{Q_{slip}^{\alpha}}{c_2 c_3 b^{\alpha 2}} \sqrt{\rho_{GND,F}^{\alpha}} \quad (18b)$$

The first terms corresponds to the initial shear resistance and the second terms are derived from the time integration of Eqs. (7a) and (7b) for the rate of shear resistance due to SSDs.

It has been discussed in (Venkataramani et al., 2007) that the initial slip system resistance in a polycrystalline aggregate depends on the grain size. The grain boundary acts as dislocation barrier and reduce the dislocation glide mean free path, which in turn contributes to the hardness through increased initial slip system shear resistance. A Hall–Petch type relation has been implemented in (Venkataramani et al., 2007) to augment the initial thermal shear resistance in (18) as:

$$\hat{s}_{*,0}^{\alpha} = s_{*,0}^{\alpha} + \frac{K^{\alpha}}{\sqrt{D_g}} \quad (19)$$

where  $D_g$  is the equivalent grain diameter and  $K^{\alpha} = \sqrt{\frac{(2-\nu)\pi\tau^* G b^{\alpha 2}}{2(1-\nu)}}$ . Here  $\nu$  is the Poissons ratio,  $G$  is the shear modulus,  $b^{\alpha}$  is the Burgers vector and  $\tau^*$  is the barrier strength for the grain boundary, which is taken as  $\tau^* = 0.01G$ .

## 2.2. Numerical implementation of crystal plasticity constitutive model

The non-local rate-dependent crystal plasticity equations in Section 2.1 are implemented in a crystal plasticity FE (CPFE) code, using an implicit time-integration scheme. The implicit scheme implements a two-step, staggered iterative approach using the backward Euler time integration methods. In the first step, local stress components, deformation and state variables, e.g.  $\mathbf{F}^p$ ,  $\dot{s}_{a,SSD}^{\alpha}$  and  $\dot{s}_{*,SSD}^{\alpha}$ , are integrated from time  $t$  to time  $t + \Delta t$  with a fixed GND density  $\rho_{GND}$  at each integration point using an iterative Newton–Raphson solver. In the second step the GND density  $\rho_{GND}$  is updated by solving the non-local Eqs. (10)–(12) in the neighborhood of each integration point. Upon achieving convergence in the two-step iteration process, the Cauchy stress  $\sigma_{ij}$  and elasto-plastic tangent stiffness matrix  $C_{ijkl}^{ep} = \frac{\partial \sigma_{ij}}{\partial E_{kl} \text{ } t+\Delta t}$  are computed and passed on to the equilibrium problem solver.

### 2.2.1. Time integration algorithm for integrating crystal plasticity constitutive equations

An implicit time integration algorithm is developed following the steps developed in (Hasija et al., 2003). In an increment from  $t$  to  $t + \Delta t$ , the algorithm seeks the solution of six nonlinear algebraic equations corresponding to the number of second Piola–Kirchoff stress components. With known values of deformation variables at time  $t$ , viz.  $\mathbf{F}(t)$ ,  $\mathbf{F}^p(t)$ ,  $s_a^{\alpha}(t)$ ,  $s_*^{\alpha}(t)$ , as well as a prescribed deformation gradient  $\mathbf{F}(t + \Delta t)$  at time  $t + \Delta t$ , the algorithm updates stresses, plastic strains and all deformation state variables, with the GND density and its rate of hardening held fixed. After convergence is reached in this step, the GNDs are updated and the procedure is repeated. Integrating Eq. (3) as:

$$\mathbf{F}^p(t + \Delta t) = \left( \mathbf{I} + \sum_{\alpha=1}^{nslip} \Delta \gamma^{\alpha} \mathbf{s}_0^{\alpha} \right) \mathbf{F}^p(t) \quad (20)$$

and substituting in Eqs. (1) and (2), yields the nonlinear equations for the updated second Piola–Kirchoff stress:

$$\mathbf{S}(t + \Delta t) = \mathbf{S}^{tr} - \sum_{\alpha=1}^{nslip} \Delta \gamma^{\alpha} (\mathbf{S}(t + \Delta t), s_a^{\alpha}(t + \Delta t), s_*^{\alpha}(t + \Delta t)) \mathbf{B}^{\alpha} \quad (21)$$

where

$$\mathbf{B}^{\alpha} = \mathbf{C} : \left[ \frac{1}{2} (\mathbf{A}(t + \Delta t) \mathbf{s}_0^{\alpha} + \mathbf{s}_0^{\alpha} \mathbf{A}(t + \Delta t)) \right] \quad (22a)$$

$$\mathbf{A}(t + \Delta t) = \mathbf{F}^{p-T}(t) \mathbf{F}^T(t + \Delta t) \mathbf{F}(t + \Delta t) \mathbf{F}^{p-1}(t) \quad (22b)$$

The nonlinear Eq. (21) is solved using Newton–Raphson iterative solver. For the  $i$ -th iteration the update in the second Piola–Kirchhoff stress is obtained as:

$$\mathbf{S}^{i+1}(t + \Delta t) = \mathbf{S}^i(t + \Delta t) - \frac{\partial \mathbf{G}}{\partial \mathbf{S}} \Big|_i^{-1} \mathbf{G}(\mathbf{S}^i(t + \Delta t)) \quad (23)$$

where  $\mathbf{G}(\mathbf{S}^i(t + \Delta t))$  is the residual defined from Eq. (21) as:

$$\mathbf{G}(\mathbf{S}^i(t + \Delta t)) = \mathbf{S}^i(t + \Delta t) - \mathbf{S}^{tr} + \sum_{\alpha=1} \Delta \gamma^\alpha \mathbf{B}^\alpha \quad (24)$$

The Jacobian matrix is:

$$\frac{\partial \mathbf{G}}{\partial \mathbf{S}^i} = \mathbf{I} + \sum_{\alpha}^{nslip} \mathbf{B}^\alpha \otimes \frac{\partial \Delta \gamma^\alpha}{\partial \mathbf{S}^i} \quad (25)$$

for which an analytical expression can be derived from Eq. (4). In this step of updating  $\mathbf{S}(t + \Delta t)$  and the increment of slip system resistance from SSDs ( $\dot{s}_{\alpha,SSD}^\alpha$  and  $\dot{s}_{\alpha,SSD}^\alpha$ ) the slip system resistance component from GNDs are held fixed.

### 2.2.2. Updating GNDs and related variables

The GNDs and associated variables are updated after reaching convergence in the solution of Eq. (23). In the hardening-based CPFPE framework, in which GNDs are not explicit variables, the GND density  $\rho_{GND}$  is evaluated from the Nye's dislocation density tensor  $\mathbf{\Lambda}$  using Eq. (15).  $\mathbf{\Lambda}$  has been defined in Eq. (10).

Numerical evaluation of  $\mathbf{\Lambda}$  requires computing the derivatives of the plastic deformation gradient at each integration point of an element. The derivatives may be numerically determined at a given point in the interior of an element, from nodal values of the variable, using element shape functions as:

$$\frac{\partial \hat{F}_{ij}^p}{\partial x_k} = \sum_{\alpha=1}^{Nnode} (\hat{F}_{ij}^p)^\alpha \frac{\partial N_\alpha}{\partial x_k} \quad (26)$$

Here  $(\hat{F}_{ij}^p)^\alpha$  are components of the nodal values of the plastic deformation gradient and  $N_\alpha$  are the element shape functions. This requires the values of  $(\hat{F}_{ij}^p)^\alpha$  at the nodal points that should be determined from those element integration point. The super-convergent patch recovery (SPR) method in (Zienkiewicz and Zhu, 1992) is deemed to be the most appropriate method for this purpose. The SPR method evaluates nodal values within a super-convergent patch  $\Omega_p$  by interpolating the variables using a higher order ( $p$ ) polynomial expansion within the patch, expressed as:

$$\tilde{F}(\mathbf{x})_{ij}^p = [\mathbf{P}(\mathbf{x})] \{\mathbf{a}\}^{ij} \quad (27)$$

where  $\tilde{F}(\mathbf{x})_{ij}^p$  represents higher order representations of plastic deformation gradient tensor components at a point  $\mathbf{x}$  in the patch,  $[\mathbf{P}(\mathbf{x})]$  is the interpolation matrix constituted of polynomial basis functions, e.g.:

$$[\mathbf{P}(\mathbf{x})] = \{1, x, y, z, x^2, y^2, z^2, xy, yz, zx, \dots\}$$

and  $\{\mathbf{a}\}^{ij}$  is the coefficient vector. A second order polynomial is used for the  $F^p$  field in this work. The coefficient vector is obtained by least-squares minimization of the difference between the function in Eq. (27) and known FEM solution  $F_{ij}^p$  at element integration points within the patch. The function to be minimized with respect to  $\{\mathbf{a}\}^{ij}$  is:

$$f(\{\mathbf{a}\}^{ij}) = \sum_{IP=1}^{N_{IP}} \left( F_{ij}^p(x, y, z) - [\mathbf{P}(x, y, z)] \{\mathbf{a}\}^{ij} \right)_{IP}^2 \quad (28)$$

where  $N_{IP}$  is the number of integration points. The minimizing solution is given in (Zienkiewicz and Zhu, 1992) as:

$$\{\mathbf{a}\}^{ij} = [\mathbf{X}]^{-1} \{\mathbf{y}\}^{ij} \quad (29)$$

where

$$\begin{aligned} [\mathbf{X}] &= \sum_{IP=1}^{N_{IP}} [\mathbf{P}(x, y, z)]_{IP}^T [\mathbf{P}(x, y, z)]_{IP} \quad \text{and} \\ \{\mathbf{y}\}^{ij} &= \sum_{IP=1}^{N_{IP}} [\mathbf{P}(x, y, z)]_{IP}^T F_{ij}^p(x, y, z)_{IP} \end{aligned} \quad (30)$$

The nodal values of each component  $F_{ij}^p$  can be evaluated using Eq. (27). The super-convergent patches can be defined separately for each grain by selecting the appropriate surrounding elements. The selection of this patch is important to avoid the ill-conditioning of the  $[\mathbf{X}]$  matrix because of the higher powers. Typically normalized coordinates are used in the construction of  $[\mathbf{P}(x, y, z)]$  (Zienkiewicz and Zhu, 1992) as:

$$\bar{x} = -1 + 2 \frac{x - x_{min}}{x_{max} - x_{min}}, \quad \bar{y} = -1 + 2 \frac{y - y_{min}}{y_{max} - y_{min}}, \quad \bar{z} = -1 + 2 \frac{z - z_{min}}{z_{max} - z_{min}} \quad (31)$$

where subscripts *max* and *min* correspond to the maximum and minimum coordinates in the patch. The normalized nodal coordinates lie within the bounds  $1 \leq \bar{x} \leq 1$ ,  $-1 \leq \bar{y} \leq 1$ , and  $-1 \leq \bar{z} \leq 1$  for nodes within a grain. A weighted least-square method is used in this work that can be used with large patches without discrimination. In this method, a weighting function that decays with the distance from the node from which the patch is being set up is used. The minimizer function in (28) is correspondingly modified as:

$$f(\{\mathbf{a}\}^{ij}) = \sum_{IP=1}^{N_{IP}} w_{IP} \left( F_{ij}^p(x, y, z) - [\mathbf{P}(x, y, z)] \{\mathbf{a}\}^{ij} \right)_{IP}^2 \quad (32)$$

where an exponentially decaying weight is chosen as  $w_{IP} = \exp(-\alpha l)$ , with  $l$  being the distance from the integration point to the target node in question and  $\alpha$  being a constant taken as 1.5 in this work.

Finally components of the Nye’s dislocation density tensor in Eq. (10) at a point in an element are evaluated as:

$$\Lambda_{ij} = \epsilon_{jsr} \frac{\partial F_{is}^p}{\partial X_r} = \epsilon_{jsr} \sum_{\alpha=1}^{N_{node}} \frac{\partial N_{\alpha}}{\partial X_r} (\hat{F}^p)_{is}^{\alpha} \quad (33)$$

where  $\epsilon_{irs}$  is the permutation tensor.

The sequence of computational operations in the crystal plasticity constitutive update procedure is provided in Table 1.

### 3. Calibration of constitutive parameters from single crystal Mg experiments

Constitutive parameters to be calibrated in the low-symmetry *hcp* crystals include: (i) reference slip system shearing rate  $\dot{\gamma}_0^z$ , (ii) initial shear resistance  $S_{*,0}^z$ , (iii) hardening rate parameters  $h_{ref}^{\beta}$  and  $r$ , (iv) reference saturation stress  $S_{sat}^{\beta}$ , and (v) parameters related to GND hardening  $c_1, c_2$  and  $c_3$ . Results of experiments and simulations in (Graff et al., 2007) suggest major dislocation activities in the basal  $\langle a \rangle$ , prismatic  $\langle a \rangle$  and 2nd order pyramidal  $\langle c + a \rangle$  slip systems for various deformation modes. This results in a total of 18 parameters to be calibrated. The strain-rate sensitivity parameter  $m$  in Eq. (4) and elastic constants have been experimentally measured in (Bhattacharya, 2006) and listed in Table 2. From a sensitivity analysis similar to that in (Hasija et al., 2003), the parameters to-be calibrated are identified to affect three experimentally observed macroscopic properties, viz. the initial macroscopic yield strength ( $\sigma_y$ ), post yield slope ( $H$ ) and macroscopic saturation stress ( $\sigma_s$ ). For each property, a genetic algorithm-based minimization is applied to determine constitutive parameters from the experimental data. The corresponding minimization statement and objective function (Xie et al., 2004) are:

$$\text{minimize} \sum_i^M \left( \sum_{j=1}^N \left( \Phi_k^{\text{experiment}} - \Phi_k^{\text{simulation}}(X_k) \right)^2 \right) \quad \forall k = 1, 2, 3 \quad (34)$$

In this equation,  $\Phi_k$ , ( $k = 1, 2, 3$ ) corresponds to an experimentally observed property. For example,  $\Phi_1 = \sigma_y$ ,  $\Phi_2 = H$  and  $\Phi_3 = \sigma_s$ . Each property  $\Phi_k$  is affected by a group of constitutive parameters  $X_i$ ,  $i = 1, 2, 3$ , i.e.  $\Phi_i = \Phi_i(X_i)$ . The constitutive parameter groups are:  $X_1 = [S_{*,0}^z, \dot{\gamma}_0^z]$ ,  $X_2 = [h_{ref}^z, r]$  and  $X_3 = [S_{sat}^z]$  is sensitive to  $\phi_3$ .  $M$  corresponds to the number of comparison experiments and  $N$  is the number of data points from each experimental result. Three experimental sets are selected for

**Table 1**

Flowchart of computational operations in constitutive update procedure.

<b>Step A</b>	Update local stress and deformation variables from $t$ to $t + \Delta t$ , with known $\mathbf{F}(t + \Delta t)$ and other variables at time $t$
i	Calculate trial second Piola–Kirchhoff stress $\mathbf{S}^{tr}$ and slip-system RSS $\tau^{\alpha tr}$ using Eqs. (21) and (5); subsequently update slip rates and deformation variables using Eqs. (6) and (7)
ii	Obtain the starting iterate $\mathbf{S}^1(t + \Delta t)$ from Eq. (21)
iii	For the $i$ -th iteration step in the Newton–Raphson algorithm: (a) Evaluate $\tau^{\alpha i} = \mathbf{S}^i(t + \Delta t) : \mathbf{s}_0^{\alpha}$ and update slip rates (b) Update $\mathbf{S}^{i+1}(t + \Delta t) = \mathbf{S}^i(t + \Delta t) - \frac{\partial \mathbf{G}}{\partial \mathbf{S}}^{-1} \mathbf{G}(\mathbf{S}^i(t + \Delta t))$ from Eqs. (22)–(25) (c) Check for convergence: if no, go back to step (a); if yes, proceed to step iv.
iv	Evaluate $\tau^{\alpha}(\mathbf{S}^{i+1}(t + \Delta t))$ and update slip system shear resistance with SSDs hardening using Eqs. (7)–(9)
v	Check for convergence of SSDs: if no, go back to step iii and compute stress with updated slip system shear resistance; if yes, proceed to step vi
vi	Evaluate $\mathbf{F}^p(t + \Delta t)$ and execute step B
vii	Calculate $\mathbf{F}^e(t + \Delta t) = \mathbf{F}(t + \Delta t) \mathbf{F}^{p-1}(t + \Delta t)$ , Cauchy stress $\boldsymbol{\sigma}(t + \Delta t) = \frac{1}{\det(\mathbf{F}^e(t + \Delta t))} \mathbf{F}^{eT}(t + \Delta t) \mathbf{S}(t + \Delta t) \mathbf{F}^e(t + \Delta t)$ and $\mathbf{C} = \frac{\partial \boldsymbol{\sigma}}{\partial \mathbf{E}} _{t+\Delta t}$
<b>Step B</b>	Update non-local deformation variables related to GNDs
i	Evaluate $\mathbf{F}^p(t + \Delta t)$ using Eq. (20) and compute nodal value of $\mathbf{F}^p(t + \Delta t)$ using Eq. (27)
ii	Compute Nye’s tensor using Eq. (33) and obtain GND density from Eq. (15)
iii	Update slip system shear resistance with GND hardening using Eqs. (16) and (18)
iv	Check for convergence in GNDs: if no, go to step A-iii with updated GNDs; if yes, proceed to step A-vii.

**Table 2**

Constitutive parameters for single crystal pure Mg; subscripts *bas*, *pri* and *pyr* correspond to basal, prismatic and 2nd order pyramidal slip systems respectively.

$C_{11}$ (GPa)	$C_{12}$ (GPa)	$C_{13}$ (GPa)	$C_{33}$ (GPa)	$C_{44}$ (GPa)
59.40	25.61	21.44	61.6	16.4
$m$	$\dot{\gamma}_0$ ( $s^{-1}$ )	$r$		
0.02	0.0023	0.25		
$(s_{\infty,0}^z)_{bas}$ (MPa)	$(s_{\infty,0}^z)_{pri}$ (MPa)	$(s_{\infty,0}^z)_{pyr}$ (MPa)		
1.4	32.5	42		
$(h_{ref}^z)_{bas}$ (MPa)	$(h_{ref}^z)_{pri}$ (MPa)	$(h_{ref}^z)_{pyr}$ (MPa)		
20	1200	2250		

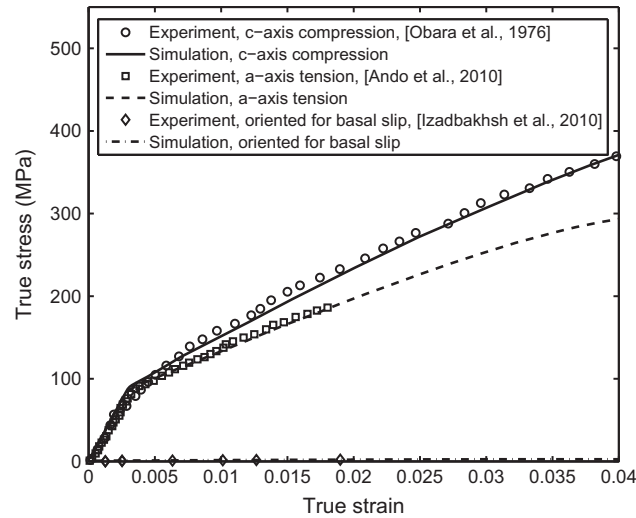


**Fig. 2.** Comparing simulation results with calibrated parameters with experimental data for single crystal pure Mg for loading in different directions. The basal slip corresponds to  $[2\bar{1}\bar{1}2]$  direction.

calibration using Eq. (34) and hence  $M = 3$ . These experiments are all conducted at room temperature under quasi-static strain-rates on bulk samples of single crystal pure Mg with nearly 100% purity. They are:

- Uniaxial compression test at 0.00016/s strain-rate along  $[0001]$  axis in (Obara et al., 1973); loading orientation maximizes the resolved shear stress on 2nd-order pyramidal  $\langle c + a \rangle$  slip system.
- Uniaxial tension at 0.00006/s strain-rate along  $[1\bar{1}20]$  direction in (Ando et al., 2010); loading orientation maximizes the resolved shear stress on the prismatic  $\langle a \rangle$  slip system.
- Tension along  $[2\bar{1}\bar{1}2]$  direction, followed by compression along the normal direction to the extruded sheet plane at 0.0002/s strain-rate in (Bhattacharya and Niewczas, 2011); loading orientation maximizes the resolved shear stress on the basal  $\langle a \rangle$  slip system.

Each of the three experiments correspond to a crystallographic orientation that favors only one slip system. Their loading orientations  $[0001]$ ,  $[1\bar{1}20]$  and  $[2\bar{1}\bar{1}2]$  are selected to maximize the resolved shear stress on the 2nd-order-pyramidal  $\langle c + a \rangle$ , prismatic  $\langle a \rangle$  and basal  $\langle a \rangle$  slip systems, respectively. Results of calibration are shown in Fig. 2 and the values of the calibrated parameters are given in Table 2. Note that the single crystal experiment in Fig. 2 had stopped before reaching the saturation regime, as opposed to the polycrystal-based experiments in (Khan et al., 2011). Consequently the value of  $s_{sat}^z$  cannot be calibrated at this step, but should be determined directly from polycrystalline simulations. Fig. 2 shows that the crystal plasticity model can capture the anisotropic plastic yielding and hardening effects in different loading directions very well. The GND parameters are calibrated with polycrystalline AZ31 experiments in selected loading modes as discussed next.

#### 4. CPFE simulation of constant strain-rate tests of polycrystalline AZ31 alloy

In this example, a crystal plasticity finite element (CPFE) model is developed to simulate response of the polycrystalline AZ31 Mg alloy under constant strain-rate loading conditions. Various steps leading to the overall objective are discussed next.

#### 4.1. 3D virtual microstructure reconstruction, meshing and mesh convergence

The CPFE simulations are conducted for statistically-equivalent virtual microstructures of the Mg alloy AZ31. These microstructural domains are constructed using the DREAM.3D software (Groeber and Jackson, 2014) that is based on methods described in (Groeber et al., 2008a,b). Virtual microstructures are generated by matching morphological and crystallographic statistics with electron back-scattered diffraction (EBSD) data obtained from focused ion beam or FIB-based serial sectioning experiments on the AZ31 alloy in (Mishra and Inal, 2013; Khan et al., 2011). The first step in virtual microstructure synthesis involves characterization (Groeber et al., 2008a), where 3D polycrystalline microstructure data is first assembled from aligned, 2D scanned images in the dual-beam FIB grain segmentation process. Following this, statistics of microstructure descriptors e.g. distribution functions of morphological parameters like grain volume, number of contiguous neighbors, aspect ratio and surface-to-volume ratio, and crystallographic parameters such as orientation, misorientation and microtexture are generated. The correlation between each parameter and grain size is also investigated. The second step involves using the distribution and correlation functions for generating statistically-equivalent synthetic 3D grain structures. A sequence of modules, viz. (i) equivalent ellipsoidal grain generator, (ii) constrained grain packer, (iii) seed point generator, (iv) constrained tessellation tool and (v) crystallographic orientation assignment is invoked for reconstructing virtual microstructures (Groeber et al., 2008b). The collection of these modules and the experimental characterization processes constitute an automated methodology for simulating representative polycrystalline microstructures.

The DREAM.3D code (Groeber and Jackson, 2014) is used to generate a  $70\ \mu\text{m} \times 70\ \mu\text{m} \times 70\ \mu\text{m}$  microstructural representative volume element or RVE containing 233 grains of the AZ31 alloy as shown in Fig. 3(a). Fig. 4 compares the statistical distributions of two representative microstructural descriptors for the reconstructed virtual microstructure and the FIB-EBSD generated 3D data respectively. The comparison of grain size (equivalent grain diameter or EGD) distribution in Fig. 4(a) shows generally good agreement with the exception at the tails. The larger grains are not adequately represented in this reconstruction. The comparison of distribution of number of contiguous neighbors for different grain-sizes in Fig. 4(b), on the other hand, is generally quite satisfactory.

A mesh convergence study is conducted with constant strain tetrahedron (CST) elements prior to simulations with the model. CPFE simulations of the microstructural RVE are conducted with the specimen loaded in uniaxial compression to a total of 2% overall strain, in a direction that is normal to the extruded sheet plane (ND). Fig. 5(a) displays the results for two mesh densities, viz. with 190,763 and 252,562 CST elements respectively. The loading direction stress  $\sigma_{33}$  is plotted along a section parallel to the z-axis at 2% strain. From the convergence of the models with two mesh densities, it is inferred that the CPFE model with 190,763 CST elements provides sufficient resolution for simulations in this study.

Furthermore, a grain convergence study is conducted to validate the sufficiency of the number of grains in the RVE (233 grains in this study) for a meaningful analysis. Two additional virtual microstructures containing 60 and 467 grains are generated from the aforementioned EBSD-FIB scanning results using DREAM.3D. Uniaxial compression tests are simulated with loading applied along ND direction and the results are plotted in Fig. 5(b). The results suggest that for the given microstructural statistics, results for the 233 and 467 grains exhibit convergence. Thus the analysis with the 233 grain microstructure is deemed sufficient.

#### 4.2. Constitutive parameter calibration for AZ31 alloy

Single crystal data for the AZ31 alloy is not generally available in the literature. Hence, the crystal plasticity constitutive parameters are calibrated from experimental data for polycrystalline AZ31 alloy. Starting with the calibrated parameters for pure Mg in Section 3, only necessary adjustments are made for the AZ31 alloy. For polycrystalline microstructure simulations, it is important to add the effect of the GNDs to the athermal and thermal shear resistances in Eqs. (8). Experimental data for the calibration is taken from (Khan et al., 2011) for quasi-static strain rate and room temperature conditions. The uniaxial compression test normal to the extruded sheet plane direction (ND), which suppresses the formation of commonly

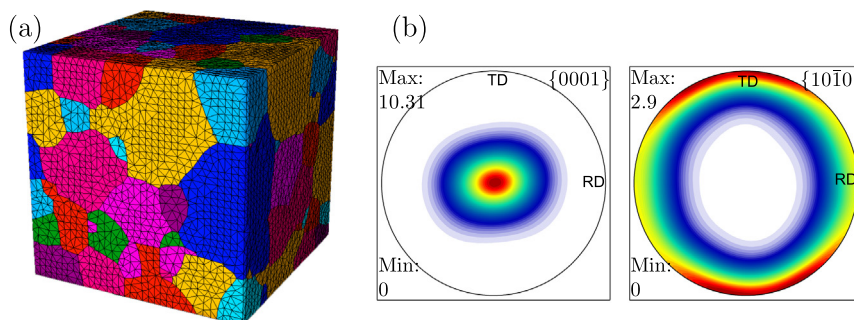
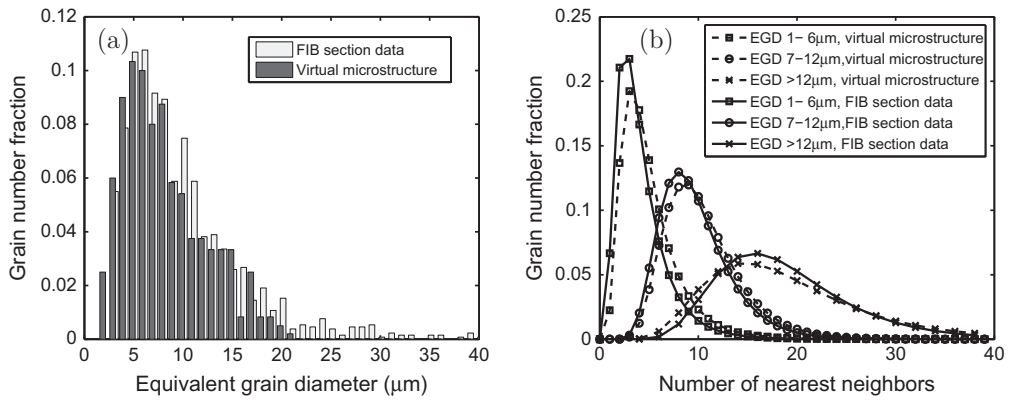
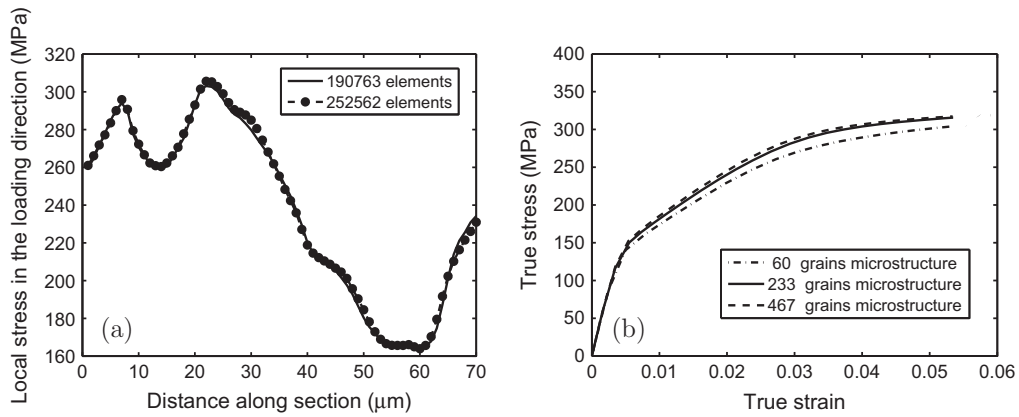


Fig. 3. (a) 3D statistically equivalent polycrystalline microstructure reconstructed from EBSD-FIB sectioning images of Mg alloy AZ31 and (b) pole figure showing initial texture assigned to the 233 grains microstructure.



**Fig. 4.** Distribution of (a) equivalent grain diameters (size) and (b) nearest neighbors for different grain sizes, for the reconstructed virtual microstructure and the FIB-EBSD generated 3D data.



**Fig. 5.** (a) Mesh convergence study with respect to the loading direction stress ( $\sigma_{33}$ ) along a section parallel to the z-axis at 2% strain and (b) convergence study on the number of grains in RVE.

**Table 3**

Crystal plasticity constitutive parameters for the alloy AZ31 with modified parameters from pure Mg to account for different chemical composition; subscripts *bas*, *pri* and *pyr* correspond to basal, prismatic and 2nd order pyramidal slip systems respectively.

$C_{11}$ (GPa)	$C_{12}$ (GPa)	$C_{13}$ (GPa)	$C_{33}$ (GPa)	$C_{44}$ (GPa)
59.40	25.61	21.44	61.6	16.4
$m$	$\dot{\gamma}_0$ ( $s^{-1}$ )	$r$		
0.02	0.0023	0.25		
$(s_{*,0}^z)_{bas}$ (MPa)	$(s_{*,0}^z)_{pri}$ (MPa)	$(s_{*,0}^z)_{pyr}$ (MPa)		
1.4	32.5	45		
$(h_{ref}^z)_{bas}$ (MPa)	$(h_{ref}^z)_{pri}$ (MPa)	$(h_{ref}^z)_{pyr}$ (MPa)	$(s_{sat}^z)_{bas}$ (MPa)	
20	800	2050	2.4	
$(s_{sat}^z)_{pri}$ (MPa)	$(s_{sat}^z)_{pyr}$ (MPa)	$c_1$	$c_2$	$c_3$
90	130	0.1	2.0	1.0

observed  $\{10\bar{1}2\}$  tension twins, is selected for validation of the dislocation glide model. The resulting constitutive parameters are listed in Table 3.

Fig. 6(a) compares the results of CPFE simulations with experiments in (Khan et al., 2011) for the AZ31 alloy. For reference, results of simulations and experiments for single crystal Mg (Obara et al., 1973) are also plotted in Fig. 6(a). The polycrystalline AZ31 simulations have reasonable agreement with experiments. In comparison with single crystal magnesium,

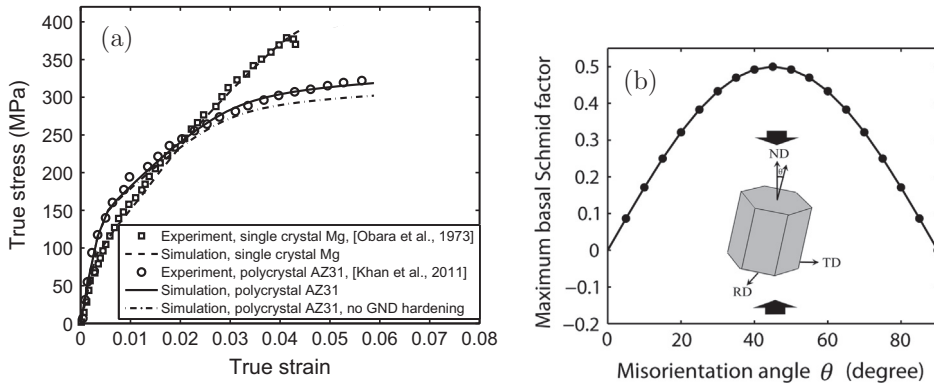


Fig. 6. (a) Comparison of simulation and experimental results for loading direction stress–strain response of polycrystalline AZ31 in uniaxial compression and (b) variation of the highest basal Schmid factor with grain rotation about RD direction ( $\theta$  is the  $c$ -axis misorientation angle from ND direction).

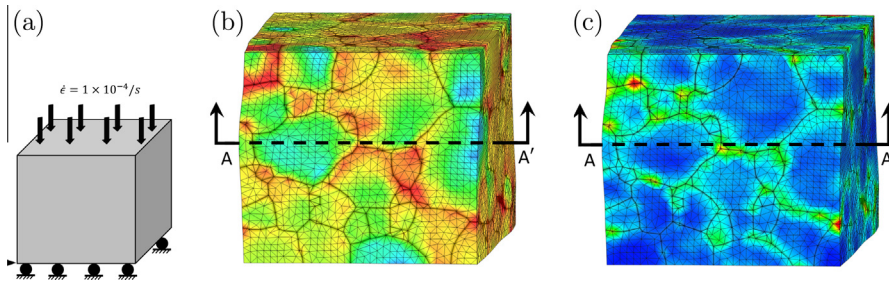


Fig. 7. (a) Schematic of boundary and loading conditions; and distribution of (b) local stress and (c) geometrically necessary dislocation (GND) density in deformed polycrystalline AZ31 at 6% strain.

the polycrystalline alloy exhibits a lower hardening rate (slope). This is primarily due to the effect of texture. Even with a  $15^\circ$  misalignment between the  $c$ -axis and loading direction, the basal  $\langle a \rangle$  Schmid factor corresponding to the easy deformation mode, can reach a value  $>0.2$ . Fig. 6(a) also shows simulation results with the contribution of GNDs excluded from slip system resistance. For this case, the last terms in Eq. (18) are removed. The comparison shows that GNDs result in a slight increase in the work hardening rate and macroscopic yield stress. This is due to the fact that GNDs only tend to accumulate close to grain boundaries where the plastic strain incompatibility occurs. Only the local stress is primarily enhanced at these locations. Variation of the highest basal  $\langle a \rangle$  system Schmid factor as a function of the  $c$ -axis misorientation from loading direction is shown in Fig. 6(b). Due to the low activation stress and hardening rate of basal slip in these grains, basal  $\langle a \rangle$  slip is activated. This results in lower macroscopic yield stress and hardening.

#### 4.3. Analysis of CPFEM simulation results for polycrystalline AZ31

Stress and GND density distributions in the polycrystalline microstructure resulting from the CPFEM simulations are analyzed in this section. The difference in the basal  $\langle a \rangle$  Schmid factor between neighboring grains leads to incompatibility induced GND concentration at grain boundaries. The loading and boundary conditions are shown in Fig. 7(a), while Fig. 7(b) and (c) depicts the contour plots of the von Mises stress and total GND density at 6% strain respectively. Difference in the slip system deformation resistances or CRSS and hardening rates, result in locally anisotropic behavior for these  $hcp$  alloys. Hard grains are nearly  $\langle c + a \rangle$  oriented with their  $[0001]$  crystal orientation close to the loading axis. Soft grains on the other hand primarily have the  $\langle a \rangle$  type slip on basal planes. The stress and GND density concentrate close to the grain boundaries, especially near those shared by hard and soft grains with large misorientations. Fig. 8(a) and (b) shows plots of the loading direction true stress and total GND density respectively, along a horizontal line A–A' through the middle section of the microstructure in Fig. 7(b). The line passes through soft–hard grain-pairs that see large gradients in the stress and GND values across the microstructure, with concentrations close to grain boundaries. In the soft grain X, the highest Schmid factor for basal slip systems is 0.4287, while that for the  $\langle c + a \rangle$  slip systems is 0.2991. Consequently basal slip dominates plastic deformation in the soft grain X, resulting in lower stresses than in other grains. In contrast, in the hard grain Y the highest Schmid factor for basal slip systems is 0.1493, while that for the  $\langle c + a \rangle$  slip systems is 0.4864. This causes dominant  $\langle c + a \rangle$  slip and high local stresses due to high yield stress and hardening rate of the  $\langle c + a \rangle$  systems. The large differences in slip-system flow rates between adjacent grains also cause crystal lattice curvature due to plastic incompatibility

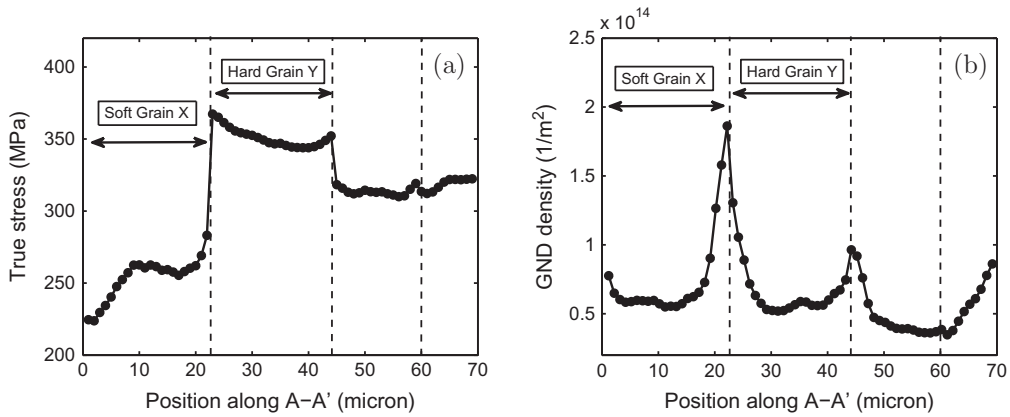


Fig. 8. Distribution of (a) true stress in the loading direction and (b) total GND density along a line A–A’ passing through a soft-hard grain boundary.

near the X–Y grain boundary leading to GND accumulation in Fig. 8(b). For a soft-hard grain pair, GNDs concentrate in the soft grain (Fig. 8(b)), while the peak stresses occur in the hard grain (Fig. 8(a)). The Schmid factor of the last two grains along A–A’ are similar and hence the stresses and GNDs do not exhibit concentration at their boundary. The stress concentrations at the soft-hard grain boundaries are responsible for twin nucleation, studied next.

5. Modeling micro-twin nucleation in polycrystalline microstructures

In this paper, twin nucleation modeling focuses on {101̄2} type twins, which are the most commonly observed twins in magnesium alloys. The {101̄2} type twins usually occupy much higher volume fraction than other twins and affects the hardening rates. Consequently, other types of twins are neglected in this study. A dislocation-assisted mechanism is assumed for the heterogeneous nucleation of {101̄2} type twins. It involves non-planar dissociation of a sessile <c + a> lattice dislocation into n layers of glissile twinning dislocations, leaving behind a residual sessile stair-rod partial dislocation for conserving the Burgers vector. Analytical studies based on elastic dislocation theory and atomistic simulations using molecular dynamic in (Ghazisaeidi and Curtin, 2013) have shown that such a dissociation process can occur under a sufficiently large applied shear stress on a 2nd order pyramidal <c + a> dislocation system {1̄21̄3} {1̄21̄2}, schematically showed in Fig. 9. The corresponding dislocation reaction is expressed as:

$$\mathbf{b}_{ini} \rightarrow \mathbf{b}_{tw} + \mathbf{b}_r \tag{35}$$

where  $\mathbf{b}_{ini} = \frac{1}{3}\langle\bar{1}2\bar{1}3\rangle$  is the Burgers vector of the initial <c + a> dislocation that dissociates into a twin partial dislocation with a net Burgers vector  $\mathbf{b}_{tw}$  and a stair-rod dislocation with a Burgers vector  $\mathbf{b}_r$ . The twin partial dislocation is  $\mathbf{b}_{tw} = ns\langle 10\bar{1}1\rangle$  where s is the magnitude of shear on each layer and n is the number of twin layers. DFT calculations and atomistic simulations in (Ghazisaeidi and Curtin, 2013) have shown that n must be larger than 6 to be stable, and a value n = 8 is taken in this study.

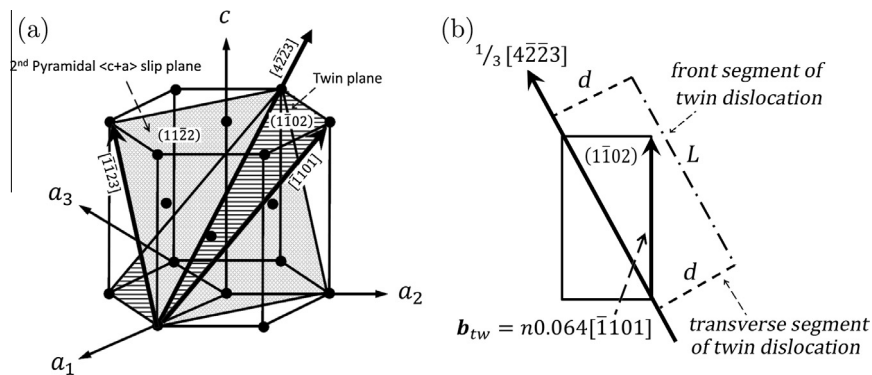


Fig. 9. Crystallographic lattice systems for 101̄2 twin nucleation: (a) <c + a> dislocation on (11̄22) plane with line direction along [4223] dissociating onto (11̄02) plane, (b) <c + a> dislocation dissociation scheme on 101̄2 twin plane.

**Table 4**Energy prefactors for Mg (unit: mJ/mm<sup>2</sup>).

$K_{tw}^{e,ft}$	$K_{tw}^{s,ft}$	$K_{tw}^{e,tr}$	$K_{tw}^{s,tr}$	$K_{ini}^e$	$K_{ini}^s$	$K_r^e$	$K_r^s$
24.7	17.3	24.7	17.3	24.2	17.7	24.5	17.3

Following (Ghazisaeidi and Curtin, 2013; Capolungo and Beyerlein, 2008), the present work extends the energetics framework using 3D elastic theory of dislocation to propose a twin nucleation criterion. Prior to dissociation, the initial energy of the system is given by the self-energy of the sessile  $\langle c + a \rangle$  dislocation as:

$$E_{ini} = \frac{L}{4\pi} \left[ K_{ini}^e (b_{ini}^e)^2 + K_{ini}^s (b_{ini}^s)^2 \right] \ln \frac{R}{r_0} \quad (36)$$

$K_{ini}$  is the elastic energy prefactor for dislocation, which is calculated using the integral method in (Hirth and Lothe, 1982). The superscript  $e$  and  $s$  refer to variables related to edge and screw dislocations respectively. Values of all energy prefactor are listed in Table 4. The scalar  $b$  denotes the magnitude of the Burgers vector, i.e.  $b = \|\mathbf{b}\| = \sqrt{(b^e)^2 + (b^s)^2}$ .  $R$  is the outer radius of the dislocation core taken as 1  $\mu\text{m}$ , while  $r_0$  is the inner radius taken as the atomic distance on basal plane, i.e.  $r_0 = 3.196 \text{ \AA}$ .  $L$  is the initial length of  $\langle c + a \rangle$  dislocation and is assumed to be 100nm. The post dissociation energy of the system is given as:

$$E_F = E_{tw} + E_r + E_{int} + E_{fault} - W_{ex} \quad (37)$$

where  $E_{tw}$  is the self-energy of the twinning dislocation loop,  $E_r$  is the self-energy of the stair-rod dislocation,  $E_{int}$  is the interaction energy between the twinning dislocation and stair-rod dislocation,  $E_{fault}$  is the stacking fault created by the twinning dislocation, and  $W_{ex}$  is the applied external work.

Following the dissociation scheme in Fig. 9(b), the self-energy of twin partial dislocation  $E_{tw}$  is evaluated by summing the line energy of front segment, transverse segment and interaction energy between transverse segments as:

$$E_{tw} = \frac{1}{4\pi} \left\{ L \left[ K_{tw}^{s,ft} (b_{tw}^{s,ft})^2 + K_{tw}^{e,ft} (b_{tw}^{e,ft})^2 \right] + 2d \left[ K_{tw}^{s,tr} (b_{tw}^{s,tr})^2 + K_{tw}^{e,tr} (b_{tw}^{e,tr})^2 \right] \right\} \ln \frac{R}{r_0} \\ - d \left\{ K_{tw}^{e,tr} \left[ \frac{(\mathbf{b}_{tw}^{e,tr} \otimes \boldsymbol{\xi}^{tr}) \cdot (\mathbf{b}_{tw}^{e,tr} \otimes \boldsymbol{\xi}^{tr})}{2\pi} \ln \frac{L}{r_0} + \frac{[(\mathbf{b}_{tw}^{e,tr} \otimes \boldsymbol{\xi}^{tr}) \cdot \mathbf{L}][(\mathbf{b}_{tw}^{e,tr} \otimes \boldsymbol{\xi}^{tr}) \cdot \mathbf{L}]}{2\pi L^2} \right] \right\} - d \left\{ K_{tw}^{s,tr} \frac{(b_{tw}^{s,tr})^2}{2\pi} \ln \frac{L}{r_0} \right\} \quad (38)$$

The superscripts  $ft$  and  $tr$  refer to the front and transverse segments of the twin partial dislocation loop. The length of the front segment of the twin partial dislocation is assumed to be the same length  $L$  as the initial  $\langle c + a \rangle$  dislocation.  $\mathbf{L}$  is the vector representation of the initial  $\langle c + a \rangle$  dislocation line. The length of transverse segment of twinning dislocation is taken as the dissociation distance  $d$ .  $\boldsymbol{\xi}^{tr}$  is the unit vector of the transverse segment of twin partial dislocation. The first part of Eq. (38) corresponds to the dislocation line energy of twin partial dislocation, while the second part corresponds to the interaction energy between its two transverse segments. No transverse segments are considered for the sessile stair-rod dislocation, and its self-energy is given as:

$$E_r = \frac{L}{4\pi} \left[ K_r^e (b_r^e)^2 + K_r^s (b_r^s)^2 \right] \ln \frac{R}{r_0} \quad (39)$$

The formation of the twin partial dislocation and stair-rod dislocation is assumed to govern the twin nucleation criterion:

$$E_{ini} \geq E_{tw} + E_r \quad (40)$$

At  $d = 0$  and conditions of isotropy, this condition reduce to the classic Frank's rule for dislocation dissociation:  $b_{ini}^2 \geq b_{tw}^2 + b_r^2$ . However actual dissociation requires a minimum energy at a finite  $d$ , i.e. the reaction products must be spatially separated as a result of internal repulsive forces. The interaction energy  $E_{int}$  is given as:

$$E_{int} = -LK_{tw}^{s,ft} \frac{(\mathbf{b}_{tw}^{s,ft} \cdot \boldsymbol{\xi}^{ft})(\mathbf{b}_r^s \cdot \boldsymbol{\xi}^r)}{2\pi} \ln \frac{d}{r_0} - LK_{tw}^{e,ft} \left\{ \frac{(\mathbf{b}_{tw}^{e,ft} \otimes \boldsymbol{\xi}^{ft}) \cdot (\mathbf{b}_r^e \otimes \boldsymbol{\xi}^r)}{2\pi} \ln \frac{d}{r_0} + \frac{[(\mathbf{b}_{tw}^{e,ft} \otimes \boldsymbol{\xi}^{ft}) \cdot \mathbf{d}][(\mathbf{b}_r^e \otimes \boldsymbol{\xi}^r) \cdot \mathbf{d}]}{2\pi d^2} \right\} \quad (41)$$

where  $\boldsymbol{\xi}^{ft}$  is the unit vector of the twin partial front segment and  $\boldsymbol{\xi}^r$  is the unit vector of the stair-rod dislocation. The first part of Eq. (41) corresponds to the interaction between stair-rod dislocation with the screw component of the twin partial front segment, while the interaction with the edge component is accommodated in the second part.

The formation of twin lamella introduces a stacking fault energy  $E_{fault}$ , which has a counter effect to the interaction energy and tends to have the two dissociation products stay close to each other. This is expressed as:

$$E_{fault} = \nu_{tw} dL \quad (42)$$

where  $\nu_{tw} = 189 \text{ mJ/mm}^2$  is the  $\{10\bar{1}2\}$  twin boundary energy. The external work done on twins under a given shear stress  $\tau_{tw}$  is:

$$W_{ext} = \tau_{tw} b_{tw} dL \quad (43)$$

After dissociation, a stable configuration can be reached at a separation distance  $d_s$ , when the final energy  $E_F$  has reached a saddle point under an applied stress, as shown in Fig. 10. The equilibrium separation distance  $d_s$  can be analytically evaluated from the conditions:

$$\frac{\partial E_F}{\partial d} = 0, \quad \frac{\partial^2 E_F}{\partial d^2} \geq 0, \quad d = d_s \quad (44)$$

Stability of the dissociated components needs to satisfy the condition:

$$E_{ini} > E_F(d = d_s, \tau_{tw}) \quad (45)$$

such that the equilibrium separation is energetically favorable and the process is irreversible.

Capolungo and Beyerlein (2008) have argued that there should be a minimum separation distance requirement on  $d_s$ , below which the elastic calculation of the dislocation self-energies are not reliable. Also, below this the cores of the initial dislocation, stair rod, and twinning partial dislocations are not distinguishable. Thus the minimum stable separation distance is assumed to be:

$$d_s > 2r_0 \quad (46)$$

Upon satisfying this criterion, it is considered that the dissociation has successfully created the twin partials and faulted areas, and thus a twin nucleus is formed.

### 5.1. Implementation of the twin nucleation criteria

The three Eqs. (40), (45) and (46) contributing to the twin nucleation criterion are examined for each of the six  $\{10\bar{1}2\}$  twin variant planes. The dissociation energy components are evaluated from Eqs. (37)–(39) and (41)–(43). For estimating the energy terms, it is necessary to know characteristics of each dislocation segment, viz. the dislocation line length  $L$ , the screw and edge components of the initial dislocation line, stair-rod dislocation and twin partial loop. These are estimated from known initial dislocation line direction and dissociation configuration, shown in Fig. 9. For a dislocation with unit line vector  $\xi$  and Burgers vector  $\mathbf{b}$ , the edge and screw components of its Burgers vector can be found as:

$$b^e = (\mathbf{b} \otimes \mathbf{n}) \cdot \xi \quad \text{and} \quad b^s = \sqrt{\|\mathbf{b}\|^2 - b^{e2}} \quad (47)$$

where  $\mathbf{n}$  is the slip plane normal. Eq. (47) is used to compute the screw and edge components of the  $\langle c + a \rangle$  dislocation, twin partial and stair-rod dislocations in the energy equations. The stable separation distance  $d_s$  in Eq. (44) is derived to be:

$$d_s = \frac{L \left[ \frac{K_{tw}^{s,ft} (\mathbf{b}_{tw}^{s,ft} \cdot \xi^{ft}) (\mathbf{b}_r^s \cdot \xi^r)}{2\pi} + \frac{K_{tw}^{e,ft} (\mathbf{b}_{tw}^{e,ft} \otimes \xi^{ft}) \cdot (\mathbf{b}_r^e \otimes \xi^r)}{2\pi} \right]}{\frac{1}{2\pi} \left[ K_{tw}^{s,tr} (b_{tw}^{s,tr})^2 + K_{tw}^{e,tr} (b_{tw}^{e,tr})^2 \right] \ln \left( \frac{R}{r_0} \right) - F_{tr} + v_{tw} L - \tau_{tw} b_{tw} L} \quad (48)$$

where

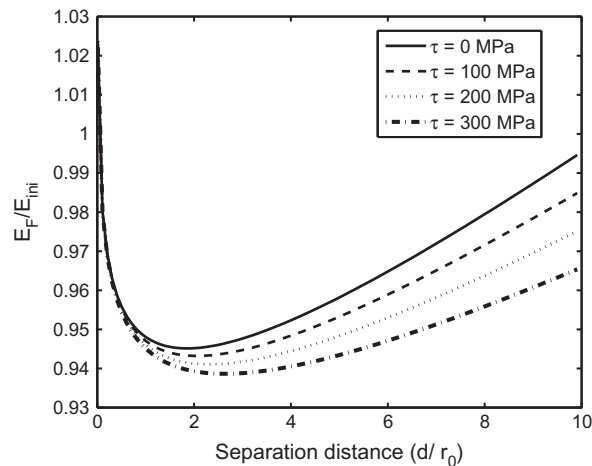


Fig. 10. Energy associated with twin nucleation event as a function of applied resolved stress and separation distance  $d$  between twin partial and stair-rod dislocations.

$$F_{tr} = K_{tw}^{e,tr} \left\{ \frac{1}{2\pi} (\mathbf{b}_{tw}^{e,tr} \otimes \xi^{tr}) \cdot (\mathbf{b}_{tw}^{e,tr} \otimes \xi^{tr}) \ln \frac{L}{r_0} + \frac{1}{2\pi L^2} [(\mathbf{b}_{tw}^{e,tr} \otimes \xi^{tr}) \cdot \mathbf{L}] [(\mathbf{b}_{tw}^{e,tr} \otimes \xi^{tr}) \cdot \mathbf{L}] \right\} + K_{tw}^{s,tr} \left[ \frac{1}{2\pi} (b_{tw}^{s,tr})^2 \ln \frac{L}{r_0} \right]$$

For each twin variant, the probability of dissociation from six  $\{\bar{1}2\bar{1}3\} \langle 1\bar{2}12 \rangle \langle c+a \rangle$  lattice dislocations is considered. Using Eqs. (40), (45) and (46), the criteria governing the formation of a twin nucleus on any twin variant is given as:

$$\begin{aligned} E_{ini} &\geq E_{tw}(d=0) + E_r \quad \text{and} \\ E_{ini} &> E_F(d_s, \tau_{tw}) \quad \forall d_s > 2r_0 \end{aligned} \tag{49}$$

5.2. CPFEM based simulations and studies on micro-twin nucleation

Simulations of polycrystalline microstructures with the CPFEM model with *a posteriori* evaluation of the micro-twin nucleation criteria are conducted in this section to validate the model and for insights on the underlying mechanisms. Comprehensive studies on the effects of microstructural statistics on micro-twin nucleation in Mg alloys have been performed in (Beyerlein et al., 2010, 2011). Their statistical analysis involves large experimental data sets (approximately 2340 grains) collected from 42 EBSD scans at different locations of the sample using an FEI XL30 field emission gun scanning electron microscope (FEG-SEM) at 20 kV with a 1 μm step size. The data is analyzed using an automated twin characterization method (Marshall et al., 2010). In the present study, the DREAM.3D code (Groeber and Jackson, 2014) is used to generate two statistically equivalent virtual microstructures (SEVM) with the same distribution of grain size, grain orientation and grain boundary misorientations as in (Beyerlein et al., 2011). The two SEVMs contain 255 and 273 grains respectively, for which the grain size, highest twin Schmid factor and misorientation distributions are compared with the experimental set in Fig. 11(a)–(c) respectively. The pole figure for a 255 grain SEVM is also provided in Fig. 11(d) to show the initial texture. For CPFEM simulations, the two SEVMs are discretized into 149,023 and 150,881 constant strain tetrahedron (CST) elements, respectively. While the statistics of the SEVMs are generally consistent with that of the experimental data, a small difference is observed due to the relatively small number of grains represented. The two virtual microstructures are used to check the effect of slightly varying statistics on the convergence of simulation results with respect to deformation and twins.

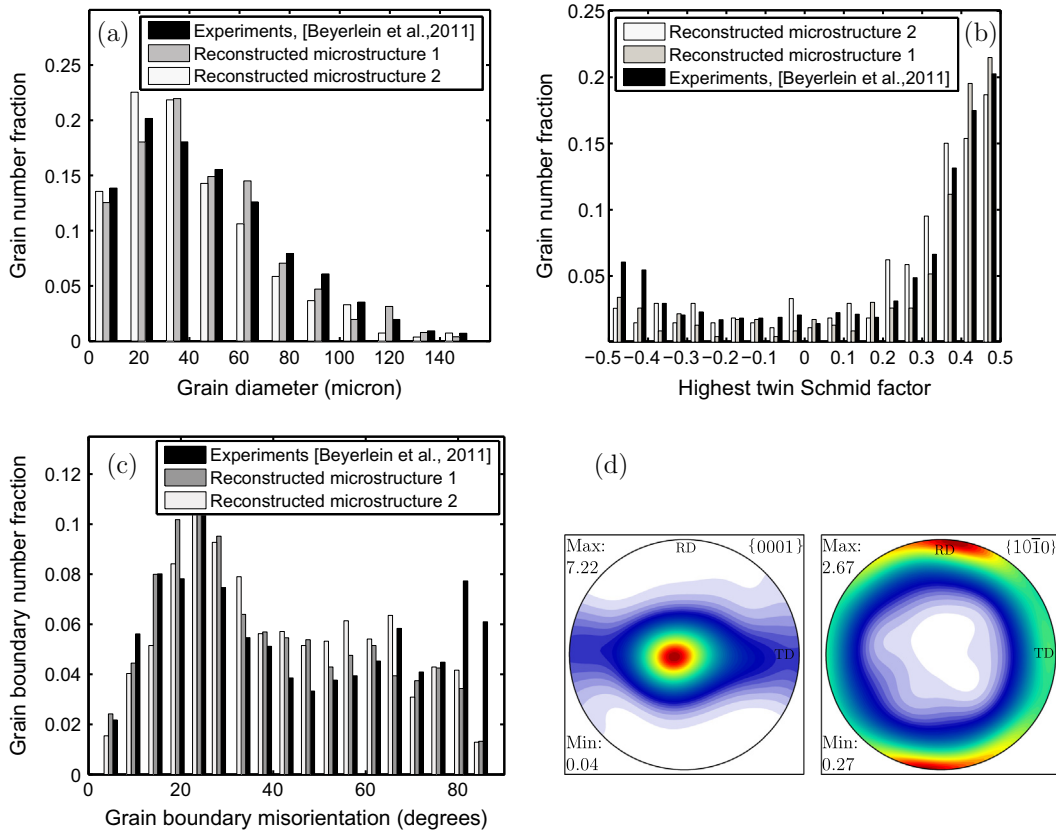


Fig. 11. Comparing statistical distributions of characteristics of the two statistically equivalent virtual microstructures (SEVMs) with experimental EBSD data-set in (Beyerlein et al., 2011) for polycrystalline Mg: (a) grain size distributions, (b) highest twin Schmid factor distributions and (c) grain boundary misorientation distributions, and (d) pole figure showing initial texture for a 255 grains virtual microstructure.

The SEVMs are subjected to compression loading in the transverse direction to the extrusion sheet plane direction (TD). For this direction, nucleation of  $\{10\bar{1}2\}$  extension twins are observed in experiments. The response is expected to be significantly different for this and other (e.g. ND) directions due to plastic anisotropy in the *hcp* alloys. A constant strain rate  $\dot{\epsilon} = 0.001/s$  is applied at a constant temperature  $T = 300$  K. The CPFEM simulations are aimed at predicting the twin nucleation sites and studying their distribution in the polycrystalline microstructure, e.g. the characteristics of grain size, orientation, grain boundary misorientation, etc. Only early stages of deformation, up to 3% strain are considered in these studies, for which experimental data is available.

### 5.2.1. Identification of twin nucleation sites in polycrystalline microstructures

Fig. 12 shows a SEVM section with a map of twin nucleation site distribution at 3.0% strain. Dark regions correspond to those that meet the twin nucleation criteria in Eqs. (49). Grain boundaries are characterized in CPFEM by the misorientation angle that is calculated using Eq. (50) between each adjacent grain pairs (Groeber et al., 2008b; Xie et al., 2004) as:

$$\theta = \min \left| \cos^{-1} \left\{ \frac{\text{tr}(\mathbf{g}_B \mathbf{g}_A^{-1} \mathbf{O}) - 1}{2} \right\} \right| \quad (50)$$

Here  $\mathbf{g}_A$  and  $\mathbf{g}_B$  are the orientation matrices of adjacent grains A and B respectively and  $\mathbf{O}$  corresponds to a crystal symmetry operator for *hcp* crystals. Details of this method are given in (Xie et al., 2004). It is possible to characterize twin nucleation sites within each grain relative to different grain boundaries, enabling direct comparison with experiments. Results of CPFEM simulations show that the primary nucleation sites are generally close to grain boundaries and triple grain boundary junctions. This observation is consistent with experimental and simulation results reported in (Beyerlein et al., 2011; Abdolvand and Daymond, 2013). Atomic scale simulations in (Wang et al., 2009) have suggested that grain boundaries are most susceptible to twin nucleation for polycrystalline Mg alloys due to dislocation pile-up induced stress concentration and existence of defect structures. Even with a uniform initial defect distribution, the constitutive model in the CPFEM simulations predicts twin nucleation sites that are observed in experiments. This suggests that twin nucleation depends on such factors as high local stress and local defect structures like grain boundaries defects (GBDs) discussed in (Beyerlein et al., 2011; Wang et al., 2009) and sessile  $\langle c + a \rangle$  dislocation in this work. The latter defects may dissociate into twin partials under local high stresses, leading to twinning. Without such defects the stress levels required to trigger homogeneous twins are extremely high, close to the theoretical yield stress level. The simulation results show some diffused twin-nucleation regions due to the fact that twin propagation is suppressed in this work.

### 5.2.2. Effect of grain size

Fig. 13(a) plots the histogram of twinned grain number fraction as a function of grain size at 3% strain. A grain that contains at least one CST element where the twin nucleation criteria (49) are satisfied is categorized as a twinned grain. The number fraction is calculated as the ratio of number of twinned grains to the total number of grains in a size range. The simulated results for both the SEVMs are in good agreement with experimental results in (Beyerlein et al., 2011). Smaller grains

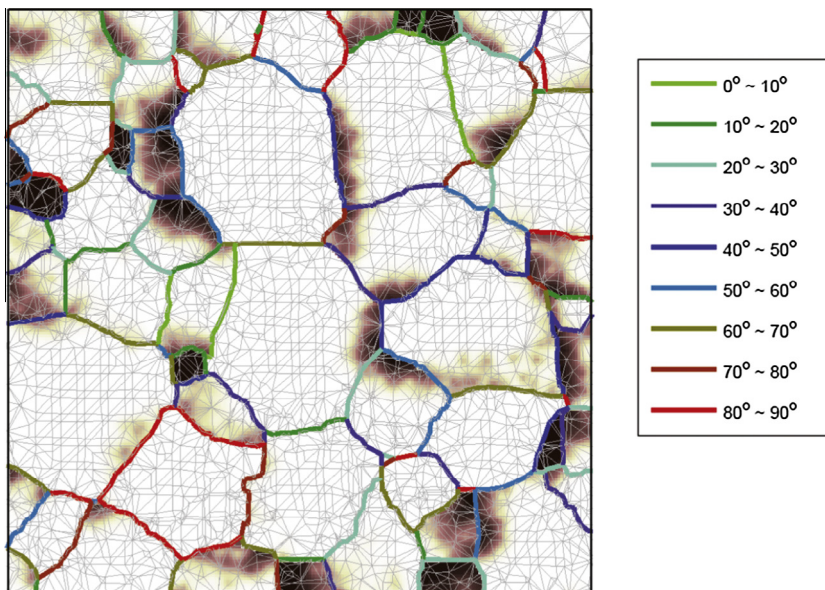


Fig. 12. A section of the virtual microstructure with a contour map of twin nucleation regions at 3% strain. Grain boundaries are color-mapped according to misorientation angles.

show a lower population of nucleated micro-twins. Meyers et al. (2001) have suggested as possible reason, a larger critical stress is necessary for twin activation in smaller grains (similar to the Hall–Petch effect for dislocation slip). However size effect is not explicitly included in the present twin nucleation model. Abdolvand and Daymond (2013) have discussed an alternative reason by correlating grain sizes with the number of adjacent grains. Bigger grains have larger grain boundaries and hence more adjacent neighbors. An increase in the number of neighbors raises the probability of finding soft-hard grain boundaries, on which stress concentrations are likely to trigger twin nucleation. Also the probability of finding triple junctions on the grain boundary increases with additional neighboring grains. From this study it can be inferred that for smaller grains, crystallographic orientation has a major influence on twinning, while for bigger grains the soft-hard grain boundaries dominate the twin nucleation process. Grain size does not have a direct effect on twin nucleation. Subsequent studies on crystallographic orientations and grain boundary are performed to investigate this conjecture.

5.2.3. Effect of crystallographic orientation

The Schmid factor of each slip or twin system may be used to represent how favorable is a grain orientation for accommodating plastic shear. The twin variant with a high Schmid factor will have high resolved shear stress and is easier to activate. The histogram of the number fraction of twinned grains at 3% strain as a function of the highest Schmid factor is plotted in Fig. 13(b). The highest twin Schmid factor in the x-axis of Fig. 13(b) is defined as the maximum Schmid factor among the six  $\{10\bar{1}2\}$  twin variants. Following (Abdolvand and Daymond, 2013), this is computed as:

$$SF^\alpha = \frac{\mathbf{s}^\alpha : \boldsymbol{\sigma}}{\|\boldsymbol{\sigma}\|} \tag{51}$$

where  $\mathbf{s}^\alpha = \mathbf{m}^\alpha \otimes \mathbf{n}^\alpha$  represents the Schmid factor of a slip or twin system  $\alpha$  and  $\boldsymbol{\sigma}$  is the Cauchy stress tensor. Depending on whether  $\boldsymbol{\sigma}$  is the local or far-field applied stress,  $SF^\alpha$  can represent the local Schmid factor (LSF) or the geometric Schmid factor (GSF). The LSF represents the effect of local stresses for a region inside a grain to twin. The GSF, on the other hand, refers to the effect of average stress for a polycrystal aggregate to twin. The comparison experiments in (Beyerlein et al., 2011) and consequently the simulations use GSF to interpret results in Fig. 13(b).

In general, good agreement is seen for both SEVM simulations with the experiments. The results show that grains with high GSF has a greater probability of nucleating a twin. However, even with a negative GSF, grains have a small probability of nucleating a twin due to locally high stress distributions. Even though some soft grains are not orientated for twin activation, the local stress state at a grain boundary with a hard grain can be favorable for twin nucleation. Consequently the local Schmid factor (LSF), computed using the local stress tensor at each integration point of an element, is plotted in Fig. 14. The results show a clear trend that points with a high LSF have a much higher twin nucleation probability, consistent with the Schmid law (Schmid and Boas, 1950).

Two key observations may be made from Fig. 14(a). The first is that not all locations with  $\sim 0.5$  LSF will twin, as the magnitude of twin system resolved shear stress may not be high enough for nucleation, especially for points located in the middle of a big grain. The second observation comes from comparing the distribution of GSF in Fig. 11(b) with that of LSF in Fig. 14(a). The number fraction of integration points with LSF  $\sim 0.5$  is much higher than that of grains with GSF  $\sim 0.5$ . This is primarily due to grain boundary constraints arising from anisotropy of different slip systems in *hcp* polycrystals. Difference in the extent of basal slip (planes of low CRSS) in neighboring grains with large misorientation can give rise to high local stress near the grain boundary, thus triggering non-basal deformation modes such as twinning and  $\langle c+a \rangle$  slip. The evolution of LSF on twin systems and basal systems are plotted in Fig. 14(b) and (c) respectively. At 0.1% strain the material is in the elastic range and no dislocation slip or twin system is activated. Since elastic anisotropy of Mg alloys is relatively small in comparison with plastic anisotropy, the stress state in each grain at 0.1% strain is close to the macroscopically averaged

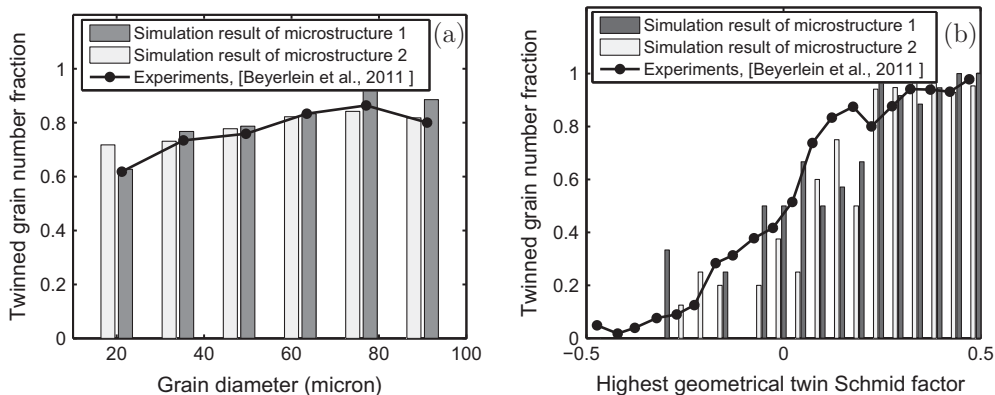


Fig. 13. Histograms of: (a) number fraction of twinned grains as a function of average grain size and (b) number fraction of twinned grains as a function of highest geometrical twin Schmid factor.

stress and hence, the distribution of LSF is similar to that of GSF in Fig. 11(b). At 0.5% strain however, basal slip is activated in several grains. The local stress state near grain boundaries start to deviate from the macroscopic stress due to the grain boundary effect, which leads to preferred deformation along the  $c$ -axis. This increases the high LSF for twin systems in Fig. 14(b) and and decreases the high LSF for basal slips in Fig. 14(c). At 2% strain, when basal slip is activated in most grains, the trend is more pronounced as shown in Fig. 14(b) and (c). The strong influence of grain orientation on twin nucleation is established in this example. Grains with high geometric twin Schmid factor have a propensity to twin, where locally the twin activation follows Schmid law.

#### 5.2.4. Effect of grain boundary

Element pairs interfacing at the same grain boundary are grouped with a misorientation measure calculated using Eq. (50), as depicted in Fig. 12. When an element associated with a grain boundary group has twinned, it is counted as a twinned boundary. The simulation results are shown in Fig. 15. To be consistent with experimental results in (Beyerlein et al., 2011), the  $c$ -axis misorientation angle between two adjacent grains is used for comparison. The simulations show the same trend as experiments, viz. the probability of twin nucleation decreases with increasing  $c$ -axis misorientation. However, as observed with simulations in (Beyerlein et al., 2011; Abdolvand and Daymond, 2013), the present CPFE simulations predict a higher probability of twin nucleation than the experiment. In (Beyerlein et al., 2011) it has been suggested that the discrepancy may be due to the fact that the experimental data statistics is derived from 2D EBSD sections that are not exactly equivalent to the statistics of 3D grain boundary structure. Also the lack of twin band propagation in the present model leads to diffusive twin nucleation behavior due to over-prediction of other nucleation sites in the same grain with deformation. This adds to the higher values of the number fraction.

In general the misorientation angle alone is insufficient for characterizing the influence of grain boundary on response, since it does not include the effect of the loading direction. Without this information, it is not feasible to identify soft-hard grain boundary in  $hcp$  crystals. As proposed in (Ghosh and Anahid, 2013; Anahid and Ghosh, 2013), a Schmid factor based indicator is proposed to characterize the soft-hard grain boundary (soft-hard grain boundary indicator), defined as:

$$SH(i, j) = \left| SF_{max}^{basal}(j) \right| - \left| SF_{max}^{basal}(i) \right| \quad (52)$$

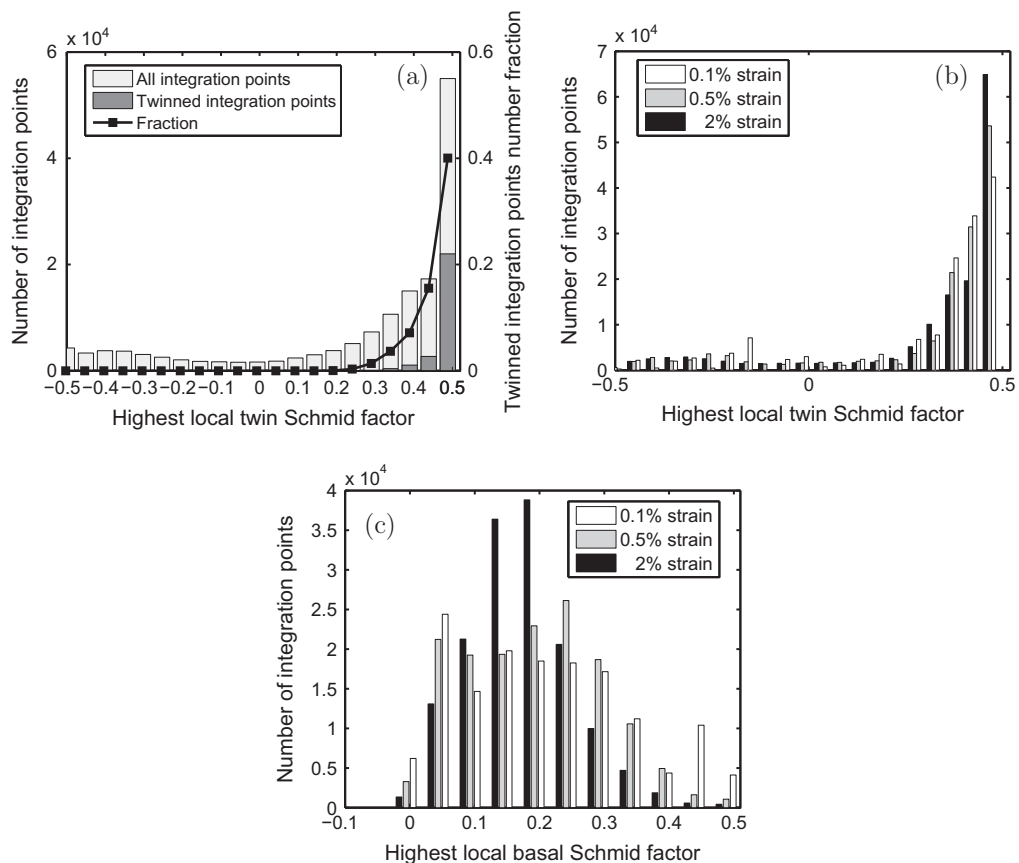


**Fig. 14.** Distribution of: (a) all grain/twinned grain as a function of highest local twin Schmid factor, (b) highest local twin system Schmid factor at different strains, and (c) highest local basal slip system Schmid factor at different strains.

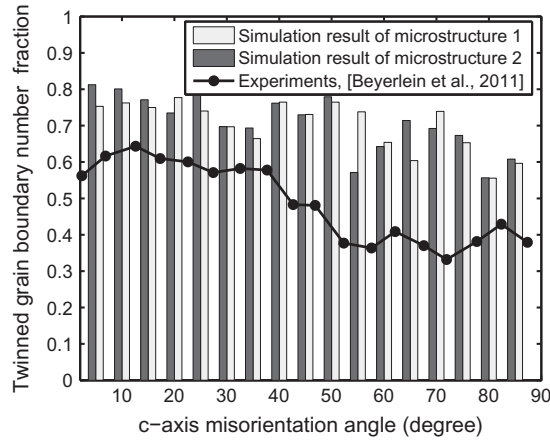


Fig. 15. Variation of twinned grain boundary number fractions with c-axis misorientation angle.

Here  $SF_{max}^{basal}(i)$  is the maximum Schmid factor among the three basal slip systems in grain  $i$  for a given loading direction. Since soft and hard grains are characterized by high and low basal Schmid factors respectively, a high positive  $SH(i,j) > 0$  represents a hard grain  $i$  neighboring a soft grain  $j$  at a hard-soft grain boundary. Conversely a high negative  $SH(i,j) < 0$  value indicates a soft-hard grain boundary on the soft grain side. Fig. 16(a) plots the distribution of twinned grain boundaries as a function of the  $SH(i,j)$  indicator. The number fraction of twinned to total grains shows a monotonic increase with the  $SH(i,j)$  indicator, from negative to positive values. Clearly, most twins tend to initiate from the hard grain side of a soft-hard grain boundary. This is because at a soft-hard grain boundary, dislocations tend to accumulate at the soft grain side causing stress concentration on the hard grain side of the grain boundary (Anahid et al., 2011). Thus for two hard grains with similar orientations, a higher local stress evolves for a softer neighboring grain, with a higher probability of twin nucleation. Introducing the Schmid factor-based  $SH(i,j)$  indicator in Fig. 16(a) allows for accounting the side of a hard-soft grain boundary in characterizing twin nucleation, as opposed to Fig. 15 where the misorientation does not discriminate between sides of the grain-boundary.

In Fig. 16(b) the number of soft-hard grain boundaries that have  $SH(i,j) \geq 0.2$  is plotted as a function of the c-axis misorientation angle. The majority of soft-hard grain boundaries lie in the misorientation range  $10^\circ$ – $50^\circ$ . This distribution corroborates observations made in Fig. 15 on a greater propensity of nucleation in the  $10^\circ$ – $50^\circ$  misorientation range. It is interesting to note that even a low misorientation angle can constitute a soft-hard grain boundary. For example in Fig. 6(b), even for a  $20^\circ$  c-axis misorientation, the basal Schmid factor is higher than 0.3 and extensive basal slip can be activated. Therefore this c-axis misorientation can contribute to a hard-soft grain pair. The basal Schmid factor reaches a maximum at  $45^\circ$  c-axis misorientation in Fig. 6(b). In the experimental samples, most grains have their c-axis aligned with the ND direction, for which a high c-axis misorientation angle ( $\geq 60^\circ$ ) exists between two soft grains with the c-axis rotated in

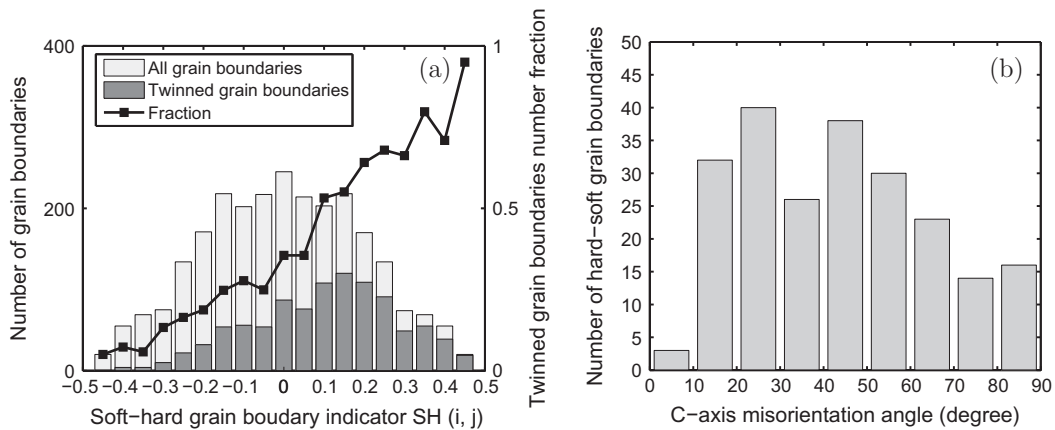


Fig. 16. Distribution of: (a) grain boundary number and twinned grain boundary fractions with soft-hard grain boundary indicator  $SH(i,j)$  (each grain boundary is considered twice from the soft grain side and hard grain side) and (b) soft-hard grain boundaries ( $SH(i,j) \geq 0.2$ ) with c-axis grain boundary misorientation angle.

opposite directions. These grain boundaries belongs to soft–soft grain boundaries and are unlikely to nucleate twins. This explains the trend of twin nucleation at low angle grain boundaries, observed in simulation and experiments.

## 6. Conclusions

This paper develops a physics-based crystal plasticity FE model of dislocation-mediated heterogeneous deformation and nucleation of  $\{10\bar{1}2\}$  micro-twins in single crystal pure magnesium and the polycrystalline alloy AZ31. The image-based computational model incorporates phenomena from a variety of experimental observations. The constitutive model for crystallographic slip incorporates both the hardening effect from evolution of statistical stored dislocations and geometrically necessary dislocations at grain boundaries driven by plastic incompatibility. The constitutive model, calibrated from pure Mg single crystal experimental data under various loading conditions, is effectively projecting strong material anisotropy in *hcp* crystals. The 3D CPFEM model incorporates polycrystalline microstructures that have equivalent statistics of morphological and crystallographic characteristics of experimental specimens. It is able to predict the macroscopic stress–strain evolution as well as the microstructural stress and GND distribution that are consistent with experimental observations.

This sets the stage for a micro-twin nucleation model that can predict the nucleation of  $\{10\bar{1}2\}$  tensile micro-twins. When subject to large applied stresses, twin nucleation is assumed to take place under conditions of dissociation of a sessile  $\langle c+a \rangle$  dislocation into a twin partial dislocation and a stair-rod dislocation. The nucleation criteria are governed by the following:

- Initial energy of the system, given as the self-energy of the sessile  $\langle c+a \rangle$  dislocation, exceeds the sum of the self-energies of the twin partial and stair-rod dislocation.
- Initial energy should be greater than the energy required to achieve a stable equilibrium configuration after dissociation, for an irreversible process.
- The dissociation distance should exceed a minimum stable separation distance.

Various CPFEM simulations are conducted to understand the effect of microstructure on twin nucleation. Specifically, the effect of three important microstructural descriptors viz. grain size, crystallographic orientation and grain boundary misorientation is investigated through simulations and validated with experiments. It is found that crystallographic orientation has a strong influence on twin nucleation. Grains with high twin Schmid factor have a much higher chance of twinning, and locally twin activation follows the Schmid law. The CPFEM results in general agree well with experiments. The interaction between neighboring grains and grain boundaries are critical in triggering twins, which tends to nucleate from the hard grain side of a soft-hard grain pair. In conclusion, the CPFEM model is found to be adequate for capturing heterogeneous deformation in the Mg family and for identifying local  $\{10\bar{1}2\}$  tensile micro-twin nucleation. It forms a good basis for modeling the twin propagation that will be discussed in a future paper.

## Acknowledgments

This work has been supported by a GOALI research program sponsored by the National Science Foundation, Mechanics and Structure of Materials Program through Grant No. CMMI-1100818 (Program Manager: Dr. Thomas Siegmund). The authors gratefully acknowledge this support. They thank their GOALI partner General Motors R&D (primary collaborator Dr. R. Mishra) for their support of this research and discussions. Computing support by the Homewood High Performance Compute Cluster (HHPC) is gratefully acknowledged.

## References

- Abdolvand, H., Daymond, M.R., 2013. Multi-scale modeling and experimental study of twin inception and propagation in hexagonal close-packed materials using a crystal plasticity finite element approach – Part I: average behavior. *J. Mech. Phys. Solids* 61, 783–802.
- Anahid, M., Ghosh, S., 2013. Homogenized constitutive and fatigue nucleation models from crystal plasticity FE simulations of Ti alloys, Part 2: macroscopic probabilistic crack nucleation model. *Int. J. Plast.* 48, 1111–1124.
- Anahid, M., Samal, M.K., Ghosh, S., 2011. Dwell fatigue crack nucleation model based on crystal plasticity finite element simulations of polycrystalline Titanium alloys. *J. Mech. Phys. Solids* 59 (10), 2157–2176.
- Ando, S., Tsushida, M., Kitahara, H., 2010. Deformation behavior of magnesium single crystal in *c*-axis compression and *a*-axis tension. *Mater. Sci. Forum* 654–656, 699–702.
- Arsenlis, A., 2001. Modeling Dislocation Density Evolution in Continuum Crystal Plasticity. Ph.D. Thesis, Massachusetts Institute of Technology.
- Arsenlis, A., Parks, D.M., 1998. Crystallographic aspects of geometrically-necessary and statistically-stored dislocation density. *Acta Mater.* 47, 1597–1611.
- Ashby, M.F., 1970. Deformation of plastically non-homogeneous materials. *Philos. Mag.* 21, 399–424.
- Barnett, L., 2007a. Twinning and the ductility of magnesium alloys: Part I: tension twins. *Mater. Sci. Eng. A* 464, 1–7.
- Barnett, L., 2007b. Twinning and the ductility of magnesium alloys: Part II. Contraction twins. *Mater. Sci. Eng. A* 464, 8–16.
- Bettles, C., Gibson, M., 2005. Material rate dependence and localized deformation in crystalline solids. *J. Miner. Met. Mater. Soc.* 57 (5), 46–49.
- Beyerlein, I.J., Capolungo, L., Marshall, P.E., McCabe, R.J., Tome, C.N., 2010. Statistical analyses of deformation twinning in magnesium. *Philos. Mag.* 90, 2161–2190.
- Beyerlein, I.J., McCabe, R.J., Tome, C.N., 2011. Effect of microstructure on the nucleation of deformation twins in polycrystalline high-purity magnesium: a multi-scale modeling study. *J. Mech. Phys. Solids* 59, 988–1003.
- Beyerlein, I.J., Tome, C.N., 2010. A probabilistic twin nucleation model for HCP polycrystalline metals. *Proc. Roy. Soc. A* 466, 2517–2544.
- Bhattacharya, B., 2006. Plastic Deformation Behavior of Pure Magnesium in the Temperature Range 4.2K–300K. Ph.D. Thesis, McMaster University.

- Bhattacharya, B., Niewczas, M., 2011. Work-hardening behaviour of Mg single crystals oriented for basal slip. *Philos. Mag.* 91, 2227–2247.
- Bohlen, J., Nurnberg, M.R., Senn, J.W., Letzig, D., Agnew, S., 2007. The texture and anisotropy of magnesium–zinc–rare earth alloy sheets. *Acta Mater.* 55, 2101–2112.
- Brown, D., Jain, A., Agnew, S., Clausen, B., 2007. Twinning and detwinning during cyclic deformation of Mg alloy AZ31B. *Mater. Sci. Forum* 539–543, 3407–3413.
- Capolungo, L.C., Beyerlein, I.J., 2008. Nucleation and stability of twins in hcp metals. *Phys. Rev. B* 78, 024117.
- Castany, P., Pettinari-Sturmel, F., Douin, J., Coujou, A., 2008. In situ transmission electron microscopy deformation of the titanium alloy Ti–6Al–4V: interface behaviour. *Mater. Sci. Eng., A* 483, 719–722.
- Deka, D., Joseph, D.S., Ghosh, S., Mills, M.J., 2006. Crystal plasticity modeling of deformation and creep in polycrystalline Ti-6242. *Metall. Trans. A* 37A (5), 1371–1388.
- Duygulu, O., Agnew, S., 2005. Plastic anisotropy and the role of non-basal slip in magnesium alloy AZ31B. *Int. J. Plast.* 21, 1161–1193.
- Ghazisaeidi, M., Curtin, W.A., 2013. Analysis of dissociation of  $\langle c \rangle$  and  $\langle c+a \rangle$  dislocations to nucleate  $\{10\bar{1}2\}$  twins in Mg. *Model. Simul. Mater. Sci. Eng.* 21, 055007.
- Ghosh, S., Anahid, M., 2013. Homogenized constitutive and fatigue nucleation models from crystal plasticity FE simulations of Ti alloys, Part 1: macroscopic anisotropic yield function. *Int. J. Plast.* 47, 182–201.
- Ghosh, S., Chakraborty, P., 2013. Microstructure and load sensitive fatigue crack nucleation in Ti-6242 using accelerated crystal plasticity FEM simulations. *Int. J. Fatigue* 48, 231–246.
- Graff, S., Brocks, W., Steglich, D., 2007. Yielding of magnesium: from single crystal to polycrystalline aggregates. *Int. J. Plast.* 23, 1957–1978.
- Groeber, M., Ghosh, S., Uchic, M.D., Dimiduk, D.M., 2008a. A framework for automated analysis and simulation of 3D polycrystalline microstructures: Part 1: statistical characterization. *Acta Mater.* 56 (6), 1257–1273.
- Groeber, M., Ghosh, S., Uchic, M.D., Dimiduk, D.M., 2008b. A framework for automated analysis and simulation of 3D polycrystalline microstructures. Part 2: Synthetic structure generation. *Acta Mater.* 56 (6), 1274–1287.
- Groeber, M.A., Jackson, M.A., 2014. DREAM.3D: a digital representation environment for the analysis of microstructure in 3D. *Integrating Mater. Manuf. Innovation* 3, 5.
- Hasija, V., Ghosh, S., Mills, M.J., Joseph, D.S., 2003. Modeling deformation and creep in Ti–6Al alloys with experimental validation. *Acta Mater.* 51, 4533–4549.
- Hirth, J.P., Lothe, J., 1982. *Theory of Dislocations*, second ed. Wiley-Interscience.
- Hutchinson, J.W., 1976. Bounds and self-consistent estimates for creep of polycrystalline materials. *Proc. Roy. Soc. Lond. A* 348, 101–127.
- Izadbakhsh, A., Inal, K., Mishra, R.K., 2012. Crystal plasticity based finite element modelling of large strain deformation in AM30 magnesium alloy. *Model. Simul. Mater. Sci. Eng.* 20, 035016.
- Izadbakhsh, A., Inal, K., Mishra, R.K., Niewczas, M., 2011. New crystal plasticity constitutive model for large strain deformation in single crystals of magnesium. *Model. Simul. Mater. Sci. Eng.* 50, 2185–2202.
- Kadiri, H.E., Kapil, J., Oppedal, A., Hector Jr., L., Agnew, S., Cherkaoui, M., Vogel, S., 2013. The effect of twintwin interactions on the nucleation and propagation of  $\{10\bar{1}2\}$  twinning in magnesium. *Acta Mater.* 61 (10), 3549–3563.
- Kadiri, H.E., Oppedal, A., 2010. A crystal plasticity theory for latent hardening by glide twinning through dislocation transmutation and twin accommodation effects. *J. Mech. Phys. Solids* 63 (7), 731736.
- Kainer, K., 2003. *Magnesium Alloys and Their Applications*. Wiley-VCH, Weinheim.
- Kaiser, F., Bohlen, J., Letzig, D., Kainer, K., Styczynski, A., Hartig, C., 2003. Influence of rolling conditions on the microstructure and mechanical properties of magnesium sheet AZ31. *Adv. Eng. Mater.* 5 (12), 891–896.
- Kelley, E.W., Hosford, W.F., 1968. Plane-strain compression of magnesium and magnesium alloy crystals. *Trans. Metall. Soc. AIME* 242, 5–13.
- Keshavarz, S., Ghosh, S., 2013. Multi-scale crystal plasticity FEM approach to modeling Nickel based superalloys. *Acta Mater.* 61, 6549–6561.
- Khan, A.S., Pandey, A., Gnaupel-Herold, T., Mishra, R.K., 2011. Mechanical response and texture evolution of AZ31 alloy at large strains for different strain rates and temperatures. *Int. J. Plast.* 27, 688–706.
- Kim, D.J., Ryu, D.Y., Bojarczuk, N.A., Karasinski, J., Guha, S., Lee, S.H., Lee, J.H., 2000. Thermal activation energies of Mg in GaN: Mg measured by the Hall effect and admittance spectroscopy. *J. Appl. Phys.* 88, 2564.
- Kock, U.F., Argon, A.S., Ashby, M.F., 1975. Thermodynamics and kinetics of slip. *Prog. Mater. Sci.* 19.
- Koehler, J.S., Seitz, F., Read, W.T.J., Shockley, W., Orowan, E., 1954. *Dislocations in Metals*, first ed. American Institute of Mining and Metallurgical Engineers, Institute of Metals Division.
- Lebensohn, R.A., Tome, C.N., 1993. A self-consistent anisotropic approach for the simulation of plastic deformation and texture development of polycrystals: application to zirconium alloys. *Acta Metall. Mater.* 41, 2611–2624.
- Lebensohn, R.A., Tome, C.N., 1994. A self-consistent viscoplastic model: prediction of rolling textures of anisotropic polycrystals. *Mater. Sci. Eng. A* 175, 71–82.
- Li, B., Ma, E., 2009. Pyramidal slip in magnesium: dislocations and stacking fault on the  $\{10\bar{1}1\}$  plane. *Philos. Mag.* 89, 1223–1235.
- Ma, A., Roters, F., Raabe, D., 2006. A dislocation density based constitutive model for crystal plasticity FEM including geometrically necessary dislocations. *Acta Mater.* 54, 2169–2179.
- Ma, Q., Kadiri, H.E., Oppedal, A., Baird, J., Horstemeyer, M., Cherkaoui, M., 2011. Twinning and double twinning upon compression of prismatic textures in an AM30 magnesium alloy. *Scr. Mater.* 64 (9), 813–816.
- Ma, Q., Kadiri, H.E., Oppedal, A., Baird, J., Horstemeyer, M., Vogel, S., 2012. Twinning effects in a rod-textured AM30 Magnesium alloy. *Int. J. Plast.* 29, 60–76.
- Marshall, P., Proust, G., Rogers, J., McCabe, R., 2010. Automatic twin statistics from electron backscattered diffraction data. *J. Microsc.* 238 (3), 218–229.
- Mendelson, S., 1970. Dislocation dissociation in hcp metals. *J. Appl. Phys.* 41 (5), 1893–1910.
- Meyers, M.A., Vohringer, O., Lubarda, V.A., 2001. The onset of twinning in metals: a constitutive description. *Acta Mater.* 49, 4025–4039.
- Mishra, R., Inal, K., 2013. *Microstructure Data*. Unpublished work.
- Molinari, A., Canova, G.R., Ahzi, S., 1987. A self consistent approach of the large deformation polycrystal viscoplasticity. *Acta Metall.* 35, 2983–2994.
- Obara, T., Yoshinga, H., Morozumi, S., 1973.  $\{11\bar{2}2\}(\bar{1}\bar{1}23)$  slip system in magnesium. *Acta Metall.* 21, 845–853.
- Oppedal, A., Kadiri, H.E., Tom, C., Kaschner, G., Vogel, S., Baird, J., Horstemeyer, M., 2012. Effect of dislocation transmutation on modeling hardening mechanisms by twinning in magnesium. *Int. J. Plast.* 3031, 41–61.
- Peirce, D., Asaro, R., Needleman, A., 1982. An analysis of nonuniform and localized deformation in ductile single crystals. *Acta Metall.* 30 (6), 1087–1119.
- Peirce, D., Asaro, R., Needleman, A., 1983. Material rate dependence and localized deformation in crystalline solids. *Acta Metall.* 31 (12), 1951–1976.
- Proust, G., Tom, C., Jain, A., Agnew, S., 2009. Modeling the effect of twinning and detwinning during strain-path changes of magnesium alloy {AZ31}. *Int. J. Plast.* 25 (5), 861–880.
- Raeisinia, B., Agnew, S., 2010. Using polycrystal plasticity modeling to determine the effects of grain size and solid solution additions on individual deformation mechanisms in cast Mg alloys. *Scr. Mater.* 58 (4), 613–624.
- Schmid, E., Boas, W., 1950. *Plasticity of Crystals*. HughesandCo.
- Serra, A., Pond, R.C., Bacon, D.J., 1991. Computer simulation of the structure and mobility of twinning dislocations in HCP metals. *Acta Metall. Mater.* 39, 1469.
- Starostsky, A., Anand, L., 2003. A constitutive model for hcp materials deforming by slip and twinning: application to magnesium alloy {AZ31B}. *Int. J. Plast.* 19 (10), 1843–1864.
- Thompson, N., Millard, D.J., 1952. Twin formation, in cadmium. *Philos. Mag.* 43, 422–440.
- Venkataramani, G., Ghosh, S., Mills, M.J., 2007. A size dependent crystal plasticity finite element model for creep and load-shedding in polycrystalline Titanium alloys. *Acta Mater.* 55, 3971–3986.

- Venkataramani, G., Kirane, K., Ghosh, S., 2008. Microstructural parameters affecting creep induced load shedding in Ti-6242 by a size dependent crystal plasticity FE model. *Int. J. Plast.* 24, 428–454.
- Wang, H., Wu, P.D., Tome, C.N., Wang, J., 2012. A constitutive model of twinning and detwinning for hexagonal close packed polycrystals. *Mater. Sci. Eng. A* 555, 93–98.
- Wang, J., Hirth, J.P., Tom, C., 2009.  $\{10\bar{1}2\}$  Twinning nucleation mechanisms in hexagonal-close-packed crystals. *Acta Mater.* 57, 5521–5530.
- Xie, C.L., Ghosh, S., Groeber, M., 2004. Modeling cyclic deformation of HSLA steels using crystal plasticity. *J. Eng. Mater. Technol.* 126, 339–352.
- Zhang, J., Joshi, S.P., 2012. Phenomenological crystal plasticity modeling and detailed micromechanical investigations of pure magnesium. *J. Mech. Phys. Solids* 60, 945–972.
- Zienkiewicz, O.C., Zhu, J.Z., 1992. The superconvergent patch recovery (SPR) and adaptive finite element refinement. *Comput. Method Appl. Mech.* 101, 207–224.